Technical Memo

ECMWF
European Centre for Medium-Range Weather Forecasts

915

SURFEM-ocean microwave surface emissivity evaluated

Alan J. Geer, Cristina Lupu, David Duncan, Niels Bormann and Stephen English
(Research Department)

February 2024

Series: ECMWF Technical Memoranda

A full list of ECMWF Publications can be found on our web site under:
http://www.ecmwf.int/en/publications/

Contact: library@ecmwf.int

Abstract

The assimilation of satellite microwave radiance observations for weather forecasting requires a model for the ocean surface emissivity. At the European Centre for Medium-range Weather Forecasts (ECMWF) the Fast Emissivity model (FASTEM) has been used for many years. A new surface emissivity model, SURFEM-ocean, is available with Radiative Transfer for TOVS (RTTOV) version 13.2 and is tested here in the context of weather forecasting. Simulations from the Integrated Forecasting System (IFS) are compared to observations. Compared to FASTEM-6, SURFEM-ocean generates better fits to observations at low frequencies (6 – 10 GHz) and in strong wind speed conditions. However, there are worse fits to observations and larger biases in mid and high frequencies (e.g. 19 – 166 GHz) especially around nadir and in horizontally polarised channels at higher zenith angles (e.g. 53°). Although the permittivity model for sea water has changed between FASTEM-6 and SURFEM-ocean, this is not a main cause of the changed surface emissivity. Instead the main explanation must be the new representation of the wind-speed dependence in SURFEM-ocean. Background departure standard deviations become fractionally worse for sensors like Advanced Microwave Sounding Unit A (AMSU-A), even in tropospheric temperature-sounding channels. However, the overall impact of moving to SURFEM-ocean is to improve weather forecasts, particularly at short range in the southern ocean. This is partly because the channels and situations that are most affected by the increase in bias, for example 90 GHz horizontally polarised channels, are not actively assimilated. A filtering effect of the data assimilation system also likely means that the effect of better performance of SURFEM-ocean in high wind speed situations at low frequencies outweighs the worse performance in other situations. However, a side effect of the changing surface emissivity biases at 37 GHz is to increase the assigned observation error for microwave imagers, and this also contributes to the apparently improved forecast scores. From a future perspective, SURFEM-ocean provides a built-in handling of all four Stokes parameters, making it able to support future full-polarimetric microwave missions such as Weather System Follow-on – Microwave (WSF-M) and Copernicus Imaging Microwave Radiometer (CIMR). Also it supports sub-millimetre applications, whereas FASTEM-6 was not valid beyond 200 GHz, and the clear improvements at 6 GHz and 10 GHz support future use of these channels for inferring sea surface temperature. Hence the decision is clearly in favour of activating SURFEM-ocean in the next operational cycle instead of FASTEM-6.

Plain Language Summary

Satellite observations contribute greatly to the quality of weather forecasts. When these observations see the ocean surface, it is necessary to model the way the ocean reflects and emits radiation at the frequency used by the satellite instrument. Knowing how things work at the ocean surface helps disentangle the information provide by the satellite measurement relating to the state of the atmosphere, the surface temperature and surface wind speed. The model of how the ocean surface affects radiation at microwave frequencies has recently been changed and is tested here against the old version of the model. The new version is not always better than the old version but it has many new capabilities that will help us make better use of future observations. In particular, future observations with higher sensitivity to sea surface temperature, surface wind speed and ice cloud will be used more accurately, which should help improve the quality of weather forecasts.

1 Introduction

Much of the satellite data assimilated at ECMWF is sensitive to the surface, and in particular the ocean surface. To assimilate this data, the observation operator requires an accurate description of the reflection and emission of radiation at the air-water interface. For a flat water surface the current description is to assume (i) specular (or direct) reflection, described by the reflectivity r, which is determined by the Fresnel equations and ultimately the permittivity of sea water and (ii) an opaque emitting surface with

a defined radiating temperature (a skin temperature) and its emissivity e given through Kirchoff's law from the reflectivity as $e = 1 - r$. In practice the ocean is not flat, due to ocean swell, wind-driven waves and capillary waves (wind-driven roughening). Further, wind and waves generate foam cover, which is strongly absorbing at microwave frequencies, in contrast to water, which is more reflective. Hence, as the wind speed increases, these additional features make the ocean surface less reflective and more emissive. Further, waves start to break the assumption of specular reflection, because downwelling radiation from many angles can be reflected into the view direction. An approximation of these effects is included in fast emissivity models, which parameterise some of the more demanding physical calculations describing wind-driven waves, and which use empirical assumptions for some of the processes that are not described physically, such as the effect of ocean foam coverage.

In operational weather forecasting, the defining fast emissivity model of the last 25 years for microwave applications has been FASTEM versions 1 to 6 (English and Hewison, 1998; Deblonde and English, 2001; Liu *et al.*, 2011; Kazumori and English, 2015). FASTEM has been provided with widely used fast radiative transfer models CRTM (Community Radiative Transfer Model; Johnson *et al.*, 2023) and RTTOV (Radiative Transfer for TOVS; Saunders *et al.*, 2020) which provides the satellite radiance observation operator at ECMWF among other forecasting centres. However, FASTEM is no longer traceable to a working physical reference model and it has known issues, for example at low microwave frequencies (Lawrence *et al.*, 2020). Kilic *et al.* (2019) also highlighted the need to improve representations of surface emissivity at low frequencies in FASTEM and other models, particularly at low surface temperatures. A further issue with FASTEM is that it has validity only up to 200 GHz, meaning it does not support upcoming sub-millimetre instruments such as Ice Cloud Imager (ICI, Eriksson *et al.*, 2020). To address the lack of modelling at higher frequencies, the TESSEM2 model was developed for RTTOV and other fast radiative transfer models (Tool to Estimate Sea-Surface Emissivity from Microwaves to sub-Millimeter waves; Prigent *et al.*, 2017). However, the microwave ocean surface emissivity community then created a new physically-based reference surface emissivity model PARMIO (Passive and Active Reference Microwave to Infrared Ocean; English *et al.*, 2020; Dinnat *et al.*, 2023) in part to address the low-frequency issues (Kilic *et al.*, 2019) as well as to provide sub-mm coverage. From the new community model, they derived a neural-network based, fast emissivity model SURFEM-ocean (Kilic *et al.*, 2023). SURFEM-ocean is included with RTTOV version 13.2. It is likely that RTTOV v14, which will be released in 2024, will support only FASTEM-6 and SURFEM-ocean.

At ECMWF, the integrated forecasting system (IFS) was updated from RTTOV v13.0 to v13.2 for cycle 49r1. Without any changes to the options, this would have been a scientifically neutral upgrade. However, given the possible benefits of SURFEM-ocean, the opportunity was taken to test the upgrade from FASTEM-6. This is the subject of the current work, following earlier tests of the impact of FASTEM-3, 4 and 5 in the IFS (Bormann *et al.*, 2011, 2012). Given the generally beneficial impact of the upgrade, and in order to be prepared for new sensors, IFS cycle 49r1 will also include the upgrade to SURFEM-ocean.

2 Method

2.1 FASTEM-6

FASTEM-6 is the end result of many developments from the original FASTEM model which will not be described in detail here (e.g English and Hewison, 1998; Deblonde and English, 2001; Liu *et al.*, 2011; Kazumori and English, 2015). The permittivity (equivalently dielectric constant) of sea water is provided by a model unique to FASTEM and frozen since version 4 (Liu *et al.*, 2011). This has been shown to

be consistent with GPM microwave imager (GMI) and Advanced Microwave Scanning Radiometer 2 (AMSR2) observations between 23 and 89 GHz but not at 19 GHz and below (Lawrence *et al.*, 2020). The permittivity is used to generate the Fresnel reflectivity of flat sea water which is then corrected for wind-driven effects, and is a function of frequency, polarisation (V and H only) and temperature.

To represent the effect of waves of all scales, there are parameterisations for large-scale and small-scale roughness. The former parameterises the output from a geometric optics model that represents the large-scale waves as an ensemble of tilted facets. The latter represents Bragg scattering and diffraction from capillary waves. These use the wave spectrum of Durden and Vesecky (1985), scaled by a factor of two in the total slope variance. Both are dependent on the near-surface (10 m) wind speed as well as frequency, polarisation and zenith angle. These are applied respectively as additive and multiplicative corrections to the Fresnel reflectivity. At this point the sea water emissivity is then determined as one minus the corrected reflectivity. The effect of foam coverage is then modelled using the Monahan and Muircheartaigh (1980) whitecapping fraction as a function of 10m wind speed, which is used to linearly combine an estimated foam emissivity with the corrected sea water emissivity.

FASTEM-6 also provides an azimuth-dependent correction term for the emissivity, modelling the effect of the rotation of the observing geometry relative to the preferred wave direction (broadly perpendicular to the wind). Hence this is a function of the angle between the azimuth angle of the satellite observation and the wind direction. For the V and H polarisations, this is based on the model of Kazumori and English (2015) which was fitted to AMSR2 observations. For the third and fourth Stokes polarisations, the model of FASTEM-3 is still used (Liu *et al.*, 2011). These are additive contributions to the final emissivity output of the model.

The corresponding final reflectivity is then one minus the final emissivity, but in V and H polarisations a further multiplicative correction is made to the reflectivity to account for non-specular effects. The final version of this parameterised correction dates from FASTEM-2 (Deblonde and English, 2001) which was still using the Cox and Munk (1954) spectrum of wave facets as a function of wind speed and uses the surface to space transmittance to estimate the downwelling hemispheric radiative flux that is being scattered into the observation line-of-sight.

2.2 SURFEM-ocean

SURFEM-ocean (Kilic *et al.*, 2023) is a model for the surface emissivity and does not represent reflectivity. It has a physical component describing the flat water surface emissivity as a function of the permittivity and neural network components (one for V and H and one for Stokes 3 and 4) that has been trained on PARMIO to represent all wind-driven effects, including large and small-scale waves and foam. The permittivity model follows Meissner and Wentz (2012). In order to derive reflectivity including a correction for non-specular effects for use in RTTOV, the same approach is used as in FASTEM-6.

The PARMIO settings used in the SURFEM-ocean neural network training are described in Kilic *et al.* (2023). PARMIO represents both large and small-scale roughness and uses the Durden and Vesecky (1985) wave spectrum with an adjusted amplitude coefficient. Foam emissivity is an adapted version of the model of Anguelova and Gaiser (2013) that has been tuned to fit a range of microwave frequencies. Foam cover is based on Monahan and Muircheartaigh (1980) but with one parameter adjusted to provide better consistency with other parameterisations.

The differences between FASTEM-6 and SURFEM-ocean may come from three sources: First, the different dielectric models. Second, the different representation of wind-driven wave and foam effects within PARMIO. Third, and beyond the scientific differences, there may also be differences due to the

quality of the functional fits employed in each model and the precise way the corrections are applied. This latter is likely to work in SURFEM's favour, given the use of a neural network to directly fit all wind-driven effects in PARMIO, and given known inaccuracies in some of the more basic functional fits used in FASTEM over the years.

2.3 Surface emissivity and reflectivity within RTTOV

All-sky microwave radiance simulations are provided by the RTTOV-SCATT (Bauer *et al.*, 2006) component of RTTOV (Saunders *et al.*, 2020). RTTOV-SCATT treats the satellite field of view as a weighted combination of two independent columns representing clear sky and cloudy skies. In the cloudy column, it solves the scattering radiative transfer equations by first using a delta-Eddington solver to estimate the full angular dependence of the radiation field, then doing a line-of-sight integration of the radiative transfer equations with scattering source terms estimated from the delta-Eddington solution. This means that the surface emissivity and reflectivity from SURFEM-ocean or FASTEM-6 are used in two places within the cloudy column.

In the delta-Eddington, the surface boundary condition describes the reflectance of the downwelling flux and the flux emittance of the surface. Hence this needs the flux emissivity $\bar{e}$ and reflectivity $\bar{r}$, which are the hemispheric integral of the emissivity $e(\theta,\phi)$ and reflectivity $r(\theta,\phi)$ divided by pi. Here, θ and ϕ represent the zenith and azimuth angles. These hemispheric flux quantities are not provided by the fast emissivity models, so it is assumed that the flux emissivity is equal to the line-of-sight emissivity provided by the fast emissivity model $\bar{e} = e(\theta_o,\phi_o)$ where θ_o and ϕ_o are the observation zenith and azimuth angles. The flux reflectivity is derived from the emissivity as $\bar{r} = 1 - \bar{e}$. For the line-of-sight integration, the standard specular reflection is used with $e(\theta_o,\phi_o)$ and $r(\theta_o,\phi_o)$ provided by the emissivity model. Hence in the the line-of-sight calculation, the reflectivity is adjusted according to the non-specular correction term that is a function of the surface to space transmittance and is common to both FASTEM-6 and SURFEM-ocean. The clear column of RTTOV-SCATT also uses this approach, though with the surface to space transmittance appropriate to the clear column.

In the IFS, surface emissivity models are given a salinity value of 35 PSU, so this assumption is also common to SURFEM-ocean and FASTEM-6 in this work.

3 Emissivity differences between FASTEM and SURFEM

Figure 1 summarises some of the main changes in surface emissivity going from FASTEM-6 to SURFEM-ocean, based on simulations for GMI using the same atmospheric and surface state from an IFS background forecast. The sample includes all locations over pure ocean (no land or sea ice) in the two assimilation cycles at 00 UTC and 12 UTC on 15th June 2020. At 10.65 and 36.5 GHz, both V and H polarised simulations have a slightly stronger dependence on 10m wind speed, compared to FASTEM-6. Emissivities are slightly smaller at zero wind speed and slightly larger at high wind speeds. In contrast, at 36.5 GHz and above, SURFEM-ocean starts to reduce the dependence on wind speed compared to FASTEM-6. The largest changes are reductions in surface emissivity that reach around 0.04 at high wind speeds, H-polarisation and high frequencies (89.0 GHz and 166.5 GHz). At these frequencies the V-polarisation emissivities increase slightly, particularly at low wind speeds. The net result is that simulated observations will be more polarised at high frequencies, with less wind dependence.

Figure 2 examines the differences as a function of sea surface (skin) temperature. The changes are

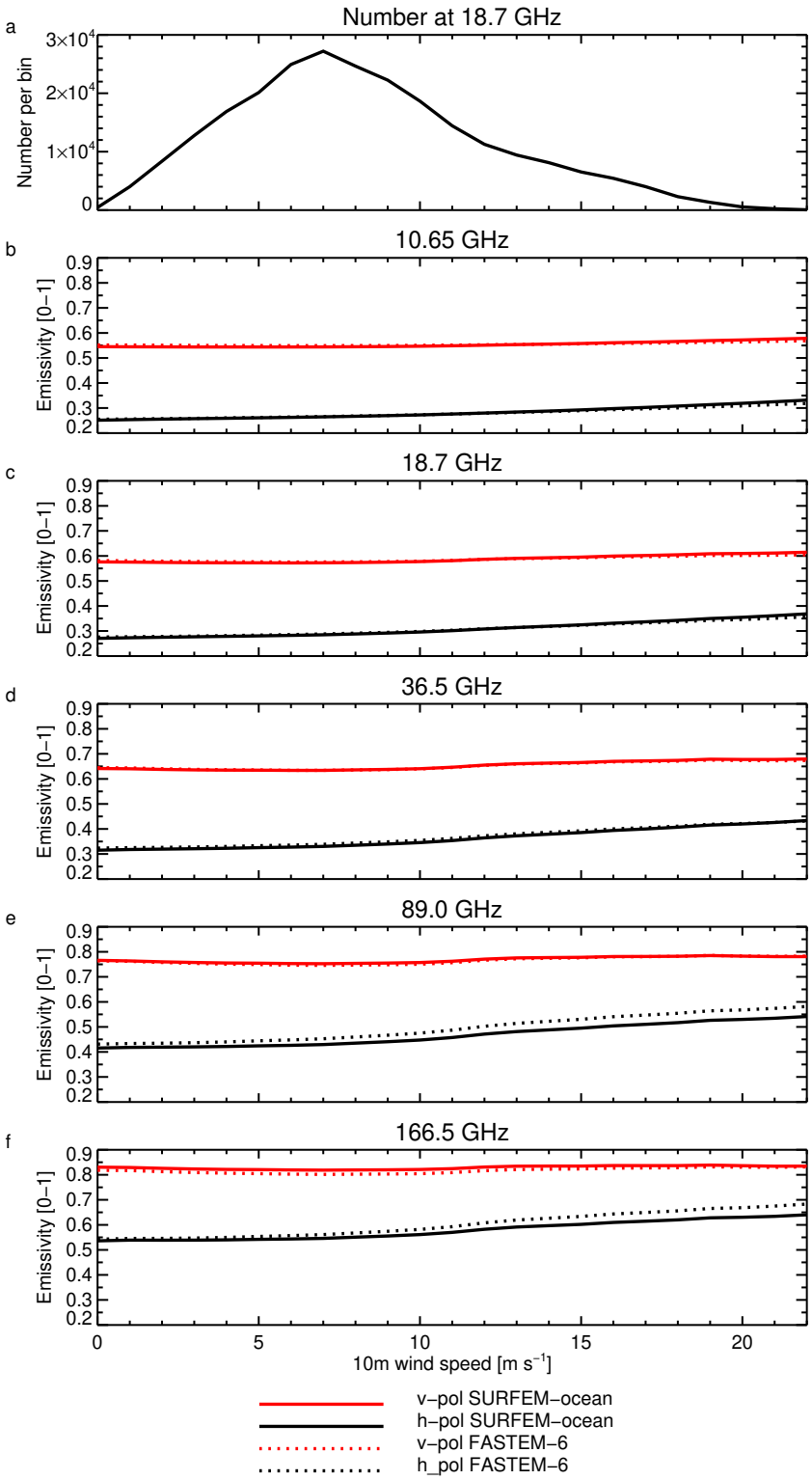

Figure 1: Microwave surface emissivity for GMI channels binned as a function of 10m wind speed, using all available observations in the assimilation windows on 15th June 2020.

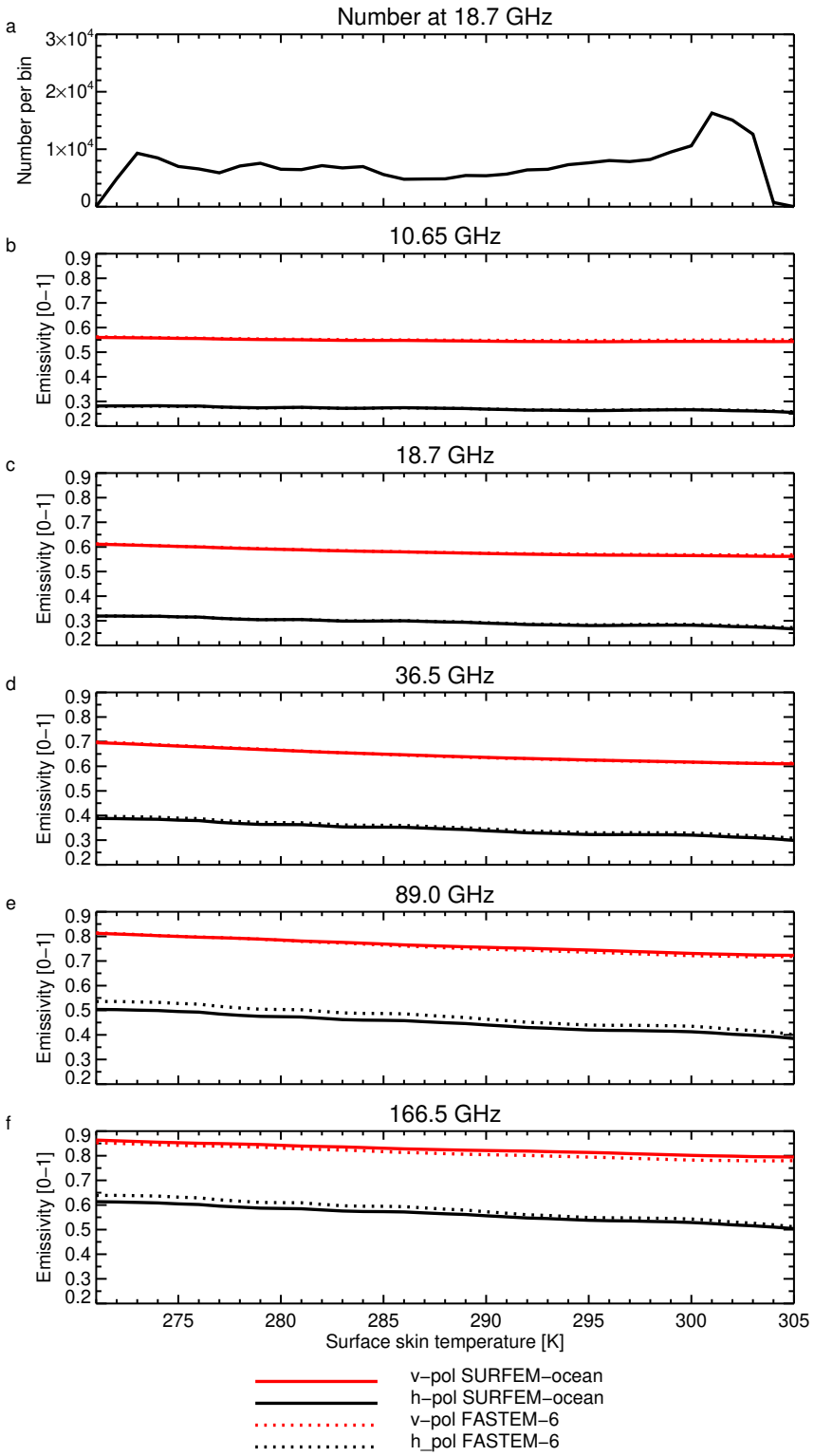

Figure 2: Microwave surface emissivity for GMI channels binned as a function of sea surface temperature, using all available observations in the assimilation windows on 15th June 2020.

much smaller and harder to see, but at 10.65 and 36.5 GHz emissivities are slightly reduced at high temperatures. At 36.5 GHz the most evident change is a small reduction in surface emissivity for H-polarisation. At 89 GHz and upwards, the sensitivity to temperature is reduced, given that emissivities get higher at high temperatures in V-polarisations and get lower at low temperatures in H-polarisations.

Figure 3 looks for changes in the relative wind direction (RWD) dependence. Here the RWD angle is defined following Kazumori and English (2015) eq. A4 (meteorological wind direction minus observation azimuth view or looking angle). In this representation, 0° corresponds to the satellite seeing the downwind (e.g. breaking) side of the waves, 90° and 270° correspond to views along the wave crests and 0° being a view of the upwind, smoother sides of the waves. The signal is small, so the figure shows the delta from the mean surface emissivity across all bins. The relative wind direction dependence is stronger in H-polarisations, and with increased emissivity for views from downwind to cross-wind (0 – 100°) and (300 – 360°, and decreased emissivity (more reflective, relatively smoother surface) with the view of the upwind side of the waves. The picture is similar at V-polarisation, but the signal is smaller and the crosswind views do not increase the polarisation so much. These figures are slightly different from the more idealised dependences on cos(RWD) and cos(2 RWD) observed by Kazumori and English (2015), likely due to the fact that all wind speeds have been combined in the same figure here, as well as the relatively small sample. SURFEM-ocean increases the amplitude of the signal at 18.7 GHz and 36.5 GHz by order 0.01 in emissivity, whereas it smooths and decreases the pattern at 89.0 GHz and 166.5 GHz for H-polarisation, by order 0.05 in emissivity. The relative wind direction changes are not further examined in this work.

3.1 Effect of changing permittivity model

The Meissner and Wentz (2012) permittivity model was chosen for SURFEM-ocean in order to improve results at very low frequencies (e.g. 7 GHz and below). However, since the permittivity model can be easily swapped in the SURFEM-ocean architecture, a version was also tested using the FASTEM permittivity model (Liu *et al.*, 2011). Figure 4 shows the change in surface emissivity for these two variants of SURFEM-ocean compared to the FASTEM-6 emissivity model. Clearly the impact of the permittivity model in the transition from FASTEM-6 to SURFEM-ocean is minor, and for example the large decreases in surface emissivity in H polarised channels at higher frequencies and higher wind speeds are mostly a result of the changing wind-speed dependence, rather than the permittivity model.

4 Validation against GMI and AMSU-A

To assess the effect of the changes in surface emissivity modelling on the fit to observations, we now analyse the background departures without any bias correction $d = y_o - y_b$ where y_o is the observed brightness temperature and y_b the brightness temperature simulated from the IFS background forecast. To assess changes in departures we use GMI because it is widely acknowledged to be the best calibrated microwave imager and because it also shows the smallest biases against the IFS (e.g. Draper *et al.*, 2015; Berg *et al.*, 2016; Lean *et al.*, 2017). Therefore the hope is that better fits to GMI should indicate genuine improvements in the quality of the surface emissivity. The sample of data is the same as used in Sec. 3 and is identical between experiments. Hence the assessment will initially use all available observations over open ocean. This means the comparison includes cold air outbreak (CAO) regions that are normally screened out due to the inability of the IFS to generate sufficient liquid water cloud and precipitation in these regions Lonitz and Geer (2015); Forbes *et al.* (2016). However, because the CAO screening

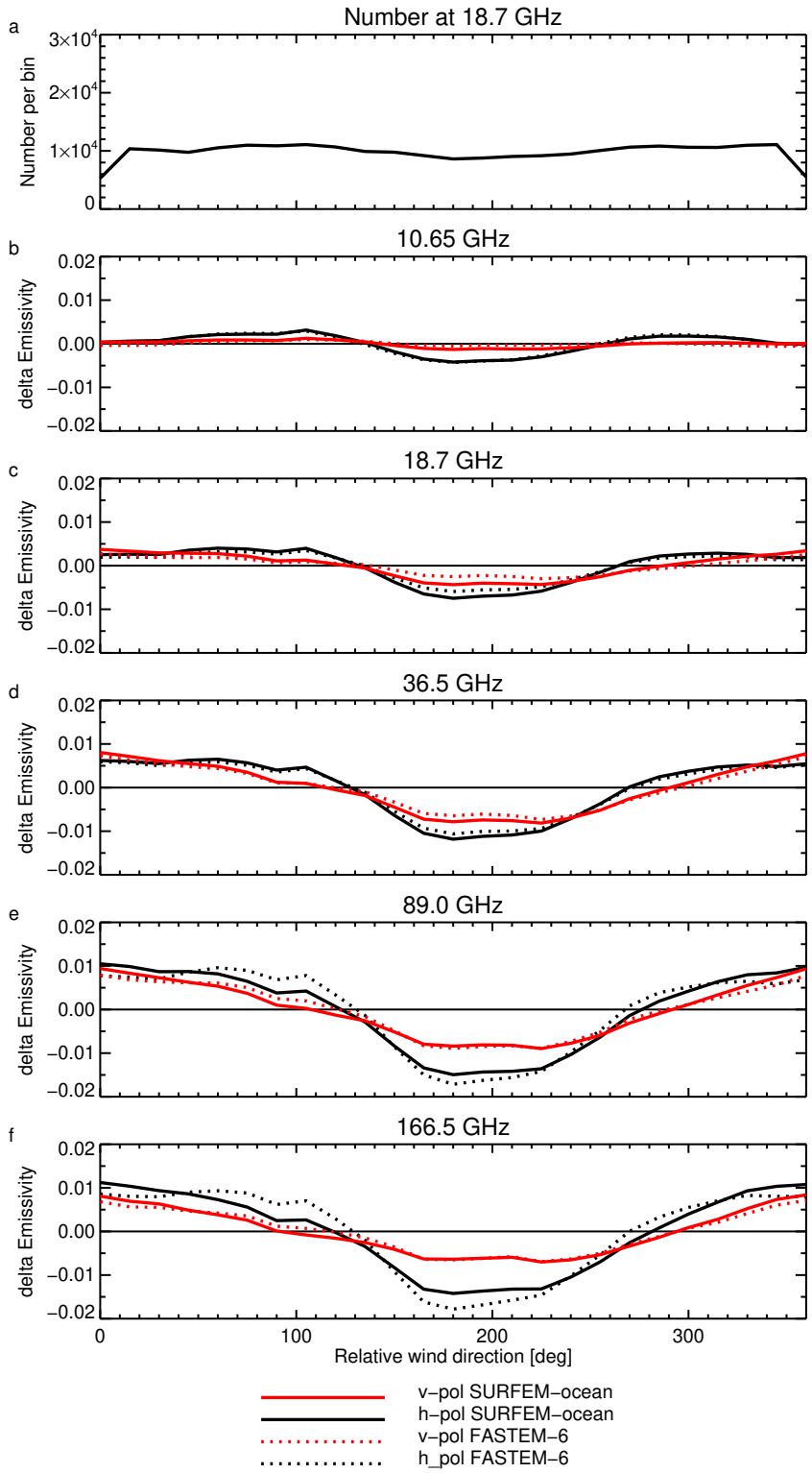

Figure 3: Microwave surface emissivity difference from mean (delta-Emissivity) for GMI channels binned as a function of relative wind direction, using all available observations in the assimilation windows on 15th June 2020.

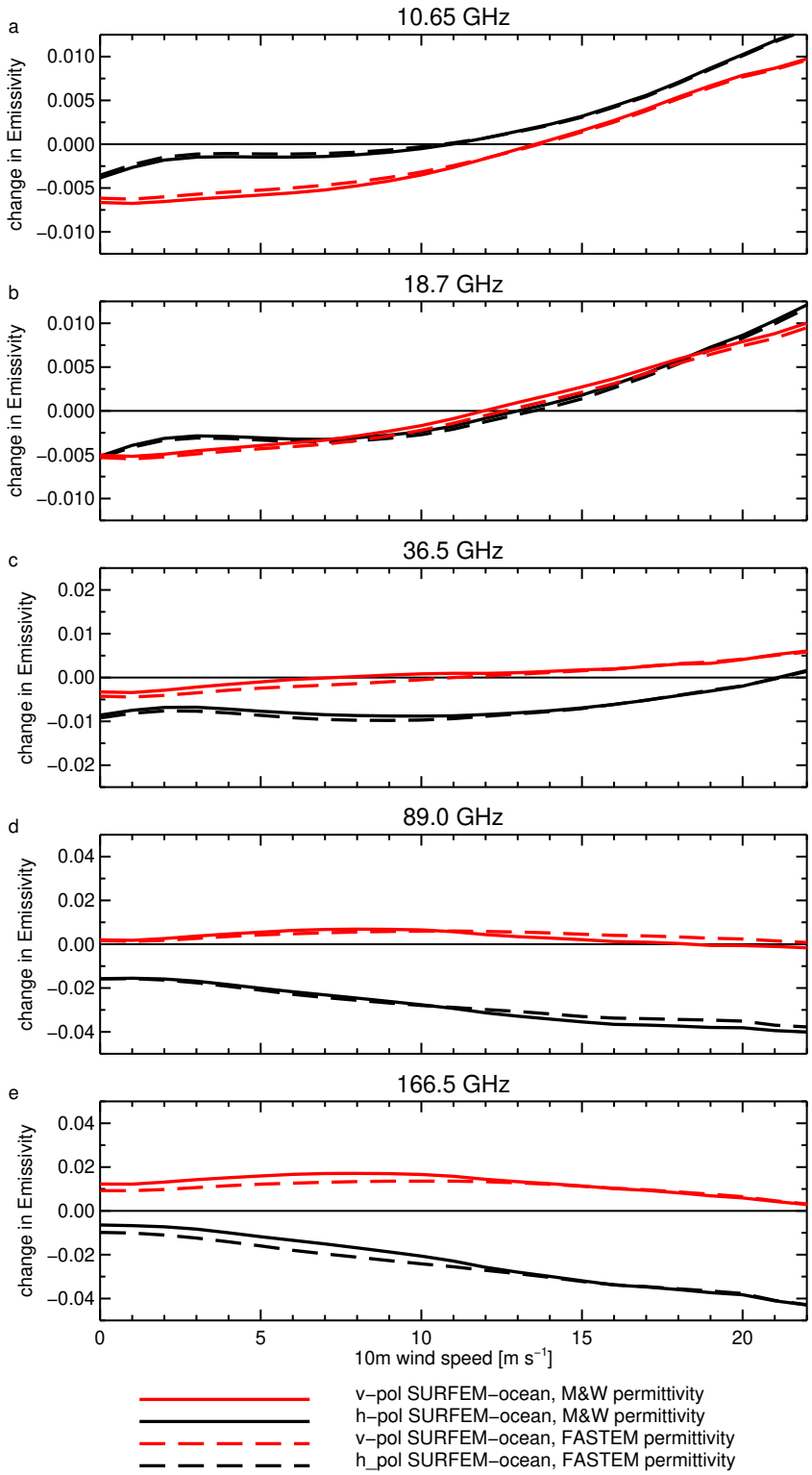

Figure 4: Using different permittivity models in SURFEM-ocean, the change in microwave surface emissivity for GMI channels binned as a function of 10m wind speed, using all available observations in the assimilation windows on 15th June 2020, compared to FASTEM-6.

removes most of the cold, high wind speed sample, it is preferred to include them in this initial analysis.

Figure 5 examines the biases as a function of near-surface wind speed. At low frequencies (10.65 GHz and 18.7 GHz) the stronger wind speed sensitivity of SURFEM-ocean generates generally a much reduced bias against GMI observations. At low wind speeds there is almost negligible bias in the V polarised channels, at between 0 and 1 K, compared to up to 2 K negative bias from FASTEM-6. At high wind speeds, in both polarisations, biases are reduced by up to around 3 K but relatively large positive biases of up to around 5 K remain. At higher frequencies (36.5 GHz and upwards) biases in V-polarisation are hardly affected, whereas in H polarisation, biases get larger by up to around 5 K in H-polarisation, reaching around 10 K, at high wind speeds.

Figure 6 shows a similar comparison but only for the observations getting past screening and data selection, i.e. the set of observations presented to the data assimilation, although some of these channels are not actively used but only monitored, in order to maintain bias corrections. The most important difference compared to Fig. 5 is the removal of the CAO regions, i.e. cold skin temperatures and often high wind speeds. At 150 GHz, this also excludes areas polewards of 45° latitude, meaning that most sensitivity to changes in surface emissivity is lost. Due to the removal of CAO regions from this sample, the biases at high wind speeds are mostly gone across the frequency range, and they reach only around 3 K. The large changes in emissivity at H-polarisation, after going to SURFEM-ocean, result in a shift towards more positive departures, particularly at 36.5 GHz and 89.0 GHz, making biases larger and smaller respectively at the two frequencies. Overall, in the screened sample, SURFEM-ocean achieves biases in most situations smaller than ± 2 K but up to +3 K at high wind speeds.

Figure 7 takes the screened sample and additionally removes cloudy scenes, using a 'symmetric' 0.05 threshold on both the observed and simulated normalised 37 GHz polarisation difference (Geer and Bauer, 2011). Using this threshold, roughly 50% of scenes are retained. The agreement between IFS and GMI is exceptionally close in most circumstances. SURFEM-ocean generates biases generally less than ± 1 K up to wind speeds of 15 m s^{-1}; zero biases are also seen at many wind speeds at higher frequencies. There are still small positive biases at high wind speeds at 10.65 GHz and 18.7 GHz, but the biases are reduced compared to FASTEM-6. If this can be considered the cleanest validation of SURFEM-ocean (though it involves discarding most of the cold surface, high wind speed data) it confirms that wind speed dependence in SURFEM-ocean is generally much better than FASTEM-6.

Figure 8 makes a similar analysis for the skin temperature dependence, here using the full observation sample including cold air outbreaks. Here, improvements in the temperature dependence are seen at 10.65 GHz and 18.7 GHz, more clearly in the V polarisation than H, though both polarisations are improved, with much flatter dependence of the bias on the skin temperature. The apparently large biases at 271 K are best ignored given the very small sample involved. Instead, the main features are the increased positive bias at 36.5 GHz, H-polarisation, seen previously, and at 89.0 GHz, substantially reduced negative bias at lower temperatures. However, at 166.5 GHz the temperature dependence seems to have got worse in the H polarisation, suggesting that the relatively large reduction in emissivity at low skin temperatures in SURFEM-ocean (Fig. 2) has made things worse.

Figure 9 briefly explores the effect of changes as a function of zenith angle using AMSU-A (Advanced Microwave Sounding Unit A, Robel, 2009) on Metop-C since GMI only sees around 53° (and slightly smaller zenith angles in the very high frequency channels). The zenith angle dependence is shown indirectly as a function of scan position, with positions 15 and 16 being near-nadir, and positions 4 and 27 representing 45° zenith angle. More extreme scan positions (high zenith angles) are eliminated in the screened sample used here, due to suspected instrument biases. The biggest changes are in the near-nadir positions in the most surface sensitive channels, 31v, 50.3v and 89v, where biases against AMSU-A have

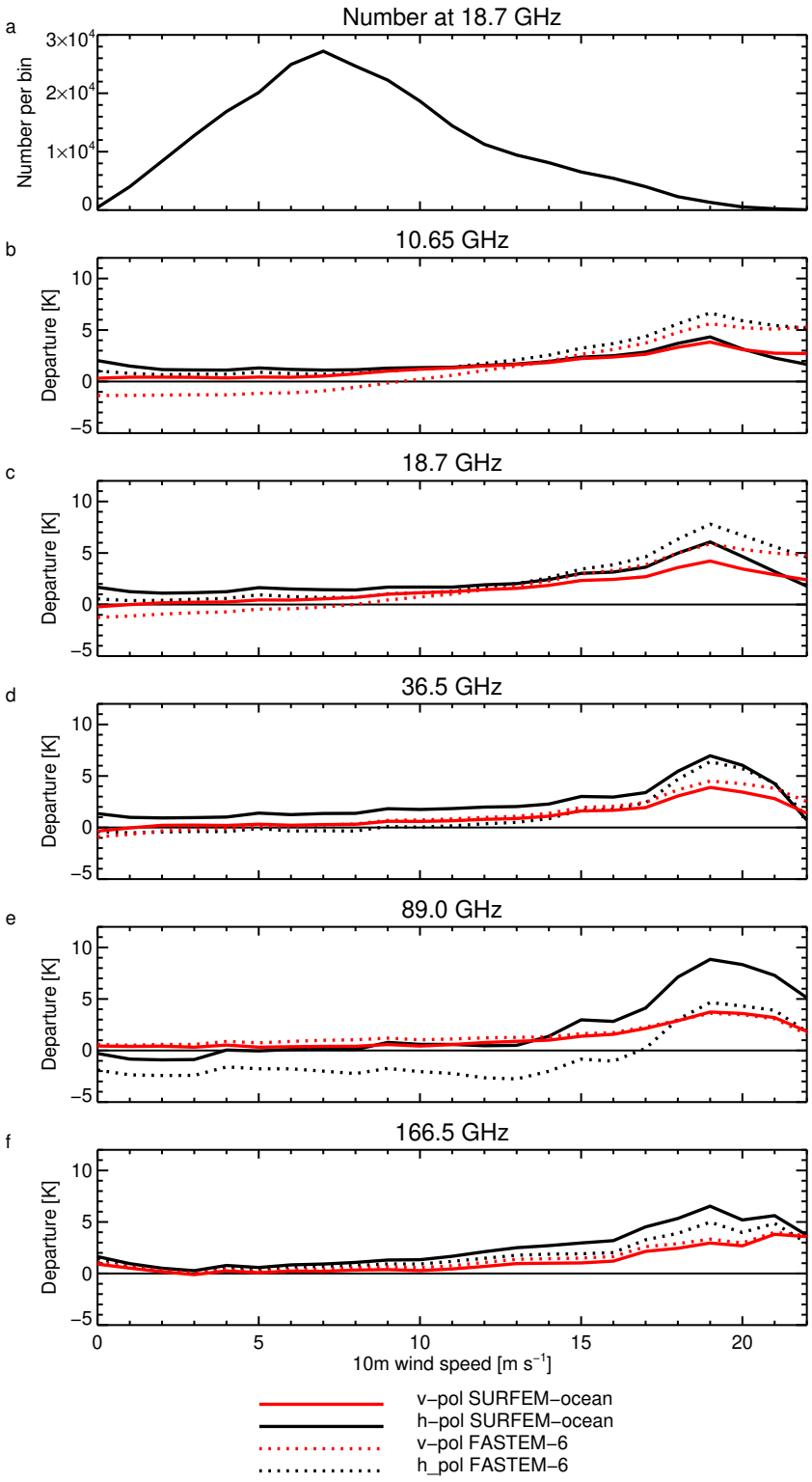

Figure 5: Background departures, before bias correction, for GMI channels binned as a function of 10m wind speed, using all available observations in the assimilation windows on 15th June 2020.

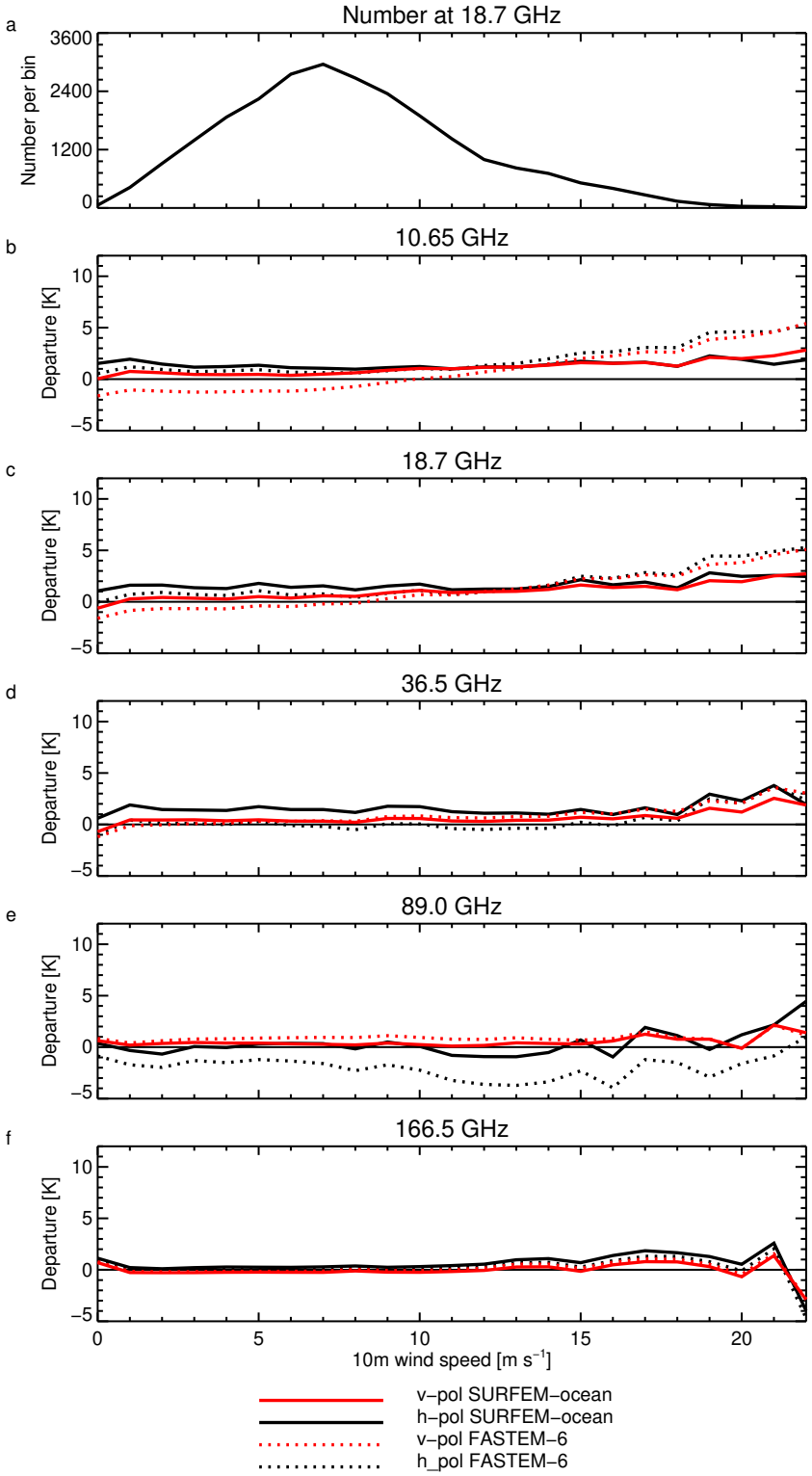

Figure 6: As Fig. 5 but using only screened observations in the assimilation windows on 15th June 2020.

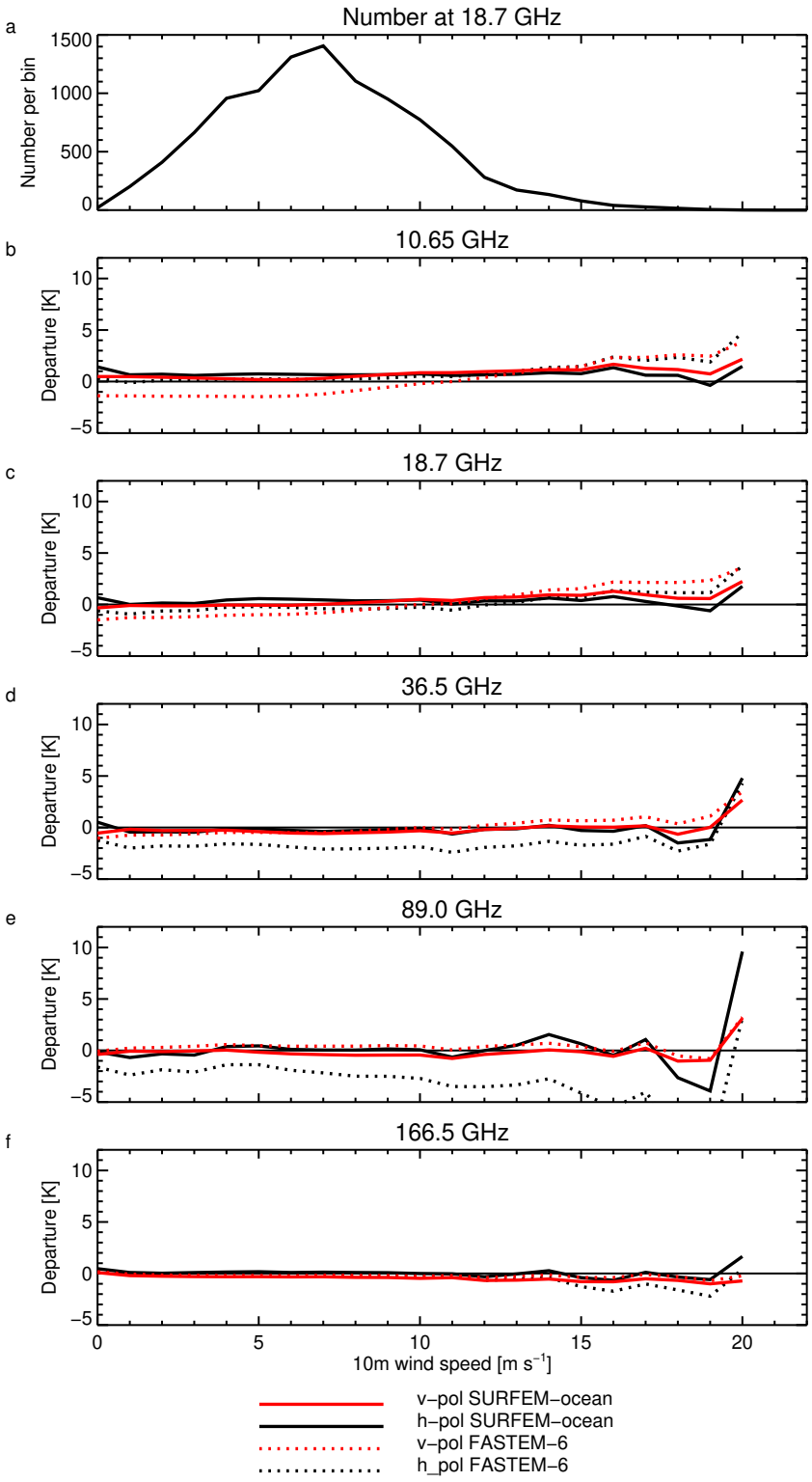

Figure 7: As Fig. 5 but using only screened and cloud-free observations in the assimilation windows on 15th June 2020.

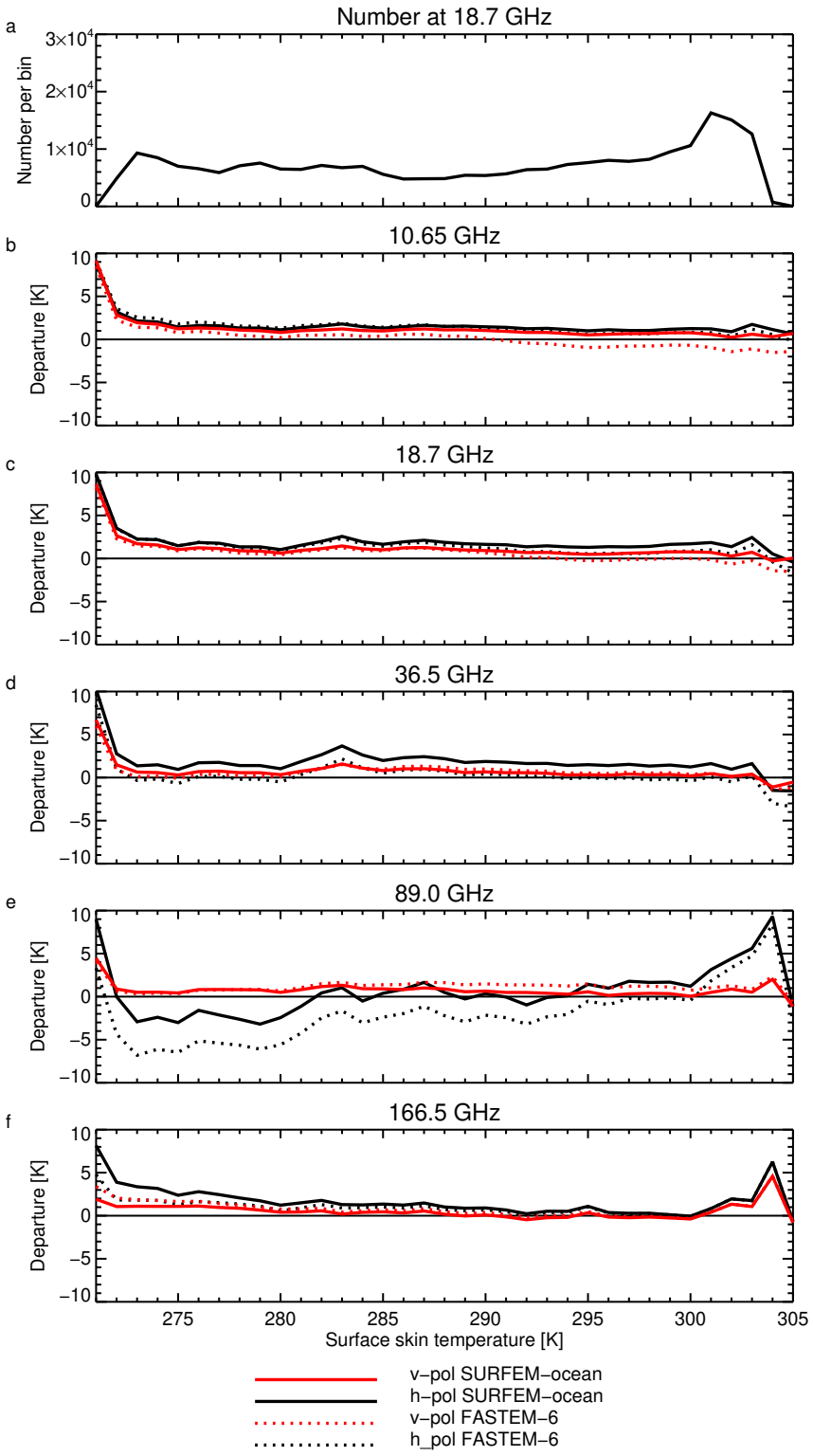

Figure 8: Background departures, before bias correction, for GMI channels binned as a function of skin temperature, using all available observations in the assimilation windows on 15th June 2020.

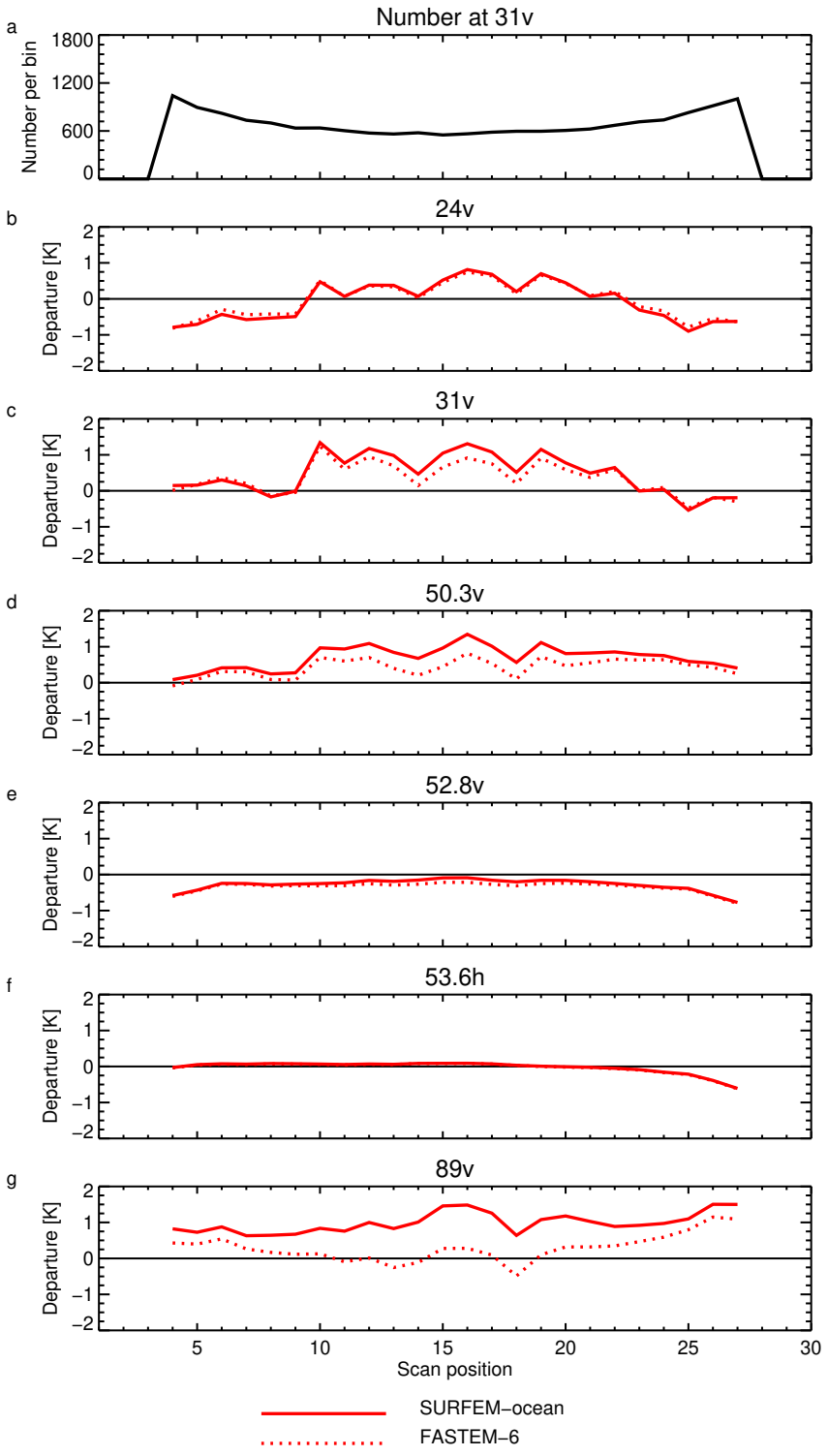

Figure 9: Background departures, before bias correction, for AMSU-A channels on Metop-C binned as a function of scan position, using screened observations in the assimilation windows on 15th June 2020.

become more positive by around 0.5 – 1.0 K, corresponding to a decrease in surface emissivity at nadir in SURFEM-ocean. Changes are smaller away from nadir. Channel 53.6h is too insensitive to the surface to show any visible changes in this presentation, but it does show very slightly increased positive biases similar to 50.3v, and there is a degradation in fit that shows up more clearly in the assimilation results given later. Note that the specified AMSU-A polarisation is for nadir, where it is irrelevant, and it rotates into a mixture of V and H off-nadir.

How far these results can be trusted as an absolute validation of SURFEM-ocean is open to question. In the cloud-free sample at screened locations (e.g. also excluding cold air outbreaks), the remaining uncertainties include the calibration of GMI, the quality of the ECMWF skin temperature, which at mid and high latitudes is derived from mainly infrared measurements, via the OSTIA analyses (Good *et al.*, 2020), and its wind speed at 10m, the validity of the opaque surface approximation, and the validity of the specular reflection assumption over rougher seas. However, in the clear-sky samples the remaining biases against GMI are typically less than ± 1 K when binned by surface wind speed (Fig. 7).

The most notable biases between SURFEM-ocean and the observations appear when the cloudy scenes are included. These features are the biases against GMI at 18.7 and 36.5 GHz of +2 K (Fig. 6), primarily in H-polarisation and against AMSU-A for nadir scenes at 31, 50.3 and 89 GHz (Fig. 9). This screened but all-sky sample is what is used in the IFS and hence these bias changes are important in understanding the data assimilation results in the next section.

In the full unscreened cloudy sample, an additional and larger issue may be the biases in the IFS clouds and precipitation, particularly in cold air outbreaks. At 36.5 GHz and above, liquid water cloud and precipitation has a very strong effect on the brightness temperatures and biases of 5 to 10 K can be explained by order 0.1 kg m^{-2} vertically integrated liquid water. Further, there is a strong known bias in this direction in the IFS water clouds in the CAO regions (Forbes *et al.*, 2016). Therefore the remaining bias peaks at strong winds in Fig. 5 at 36.5 GHz and above, which mostly go away when CAO are screened (Fig. 6), could be entirely explained by the missing liquid water cloud. Particularly at cold temperatures and strong winds (Figs. 2 and 1) the H-polarised SURFEM-ocean emissivities are strongly reduced compared to FASTEM-6. If this is physically correct, it acts to make the positive bias coming from missing CAO liquid cloud even more prominent than it was before.

However, this theory does not hold at lower frequencies, particularly 10.65 GHz, where the improved wind-dependence of SURFEM-ocean has reduced the biases but not eliminated them. In Fig. 5 there are still biases in V and H polarisations, peaking around +5 K at 19 m s^{-1} wind speed. At 10.65 GHz, sensitivity to liquid water cloud is very small, so the surface radiative transfer would be the likeliest explanation for the bias. This suggests that SURFEM-ocean (and behind it, PARMIO) could be further improved in strong wind situations. For example, the sea state is not an instantaneous and direct function of 10 m wind speed, and in this line, efforts have been made to incorporate more sophisticated wave modelling into the estimation of surface emissivity (Meunier *et al.*, 2014). Additionally, the explanation could lie in the treatment of non-specular reflection in RTTOV, which is unchanged since FASTEM-3 (Liu *et al.*, 2011) and applies equally to FASTEM-6 and SURFEM-ocean. Alternatively, if the 10m wind speeds in the IFS have errors, this could also contribute to any issues.

5 Data assimilation results

The impact of the change to SURFEM-ocean in data assimilation is slightly different to the validation exercise in the previous section, for several reasons. First, many of the biases of the surface emissivity model are already corrected by variational bias correction (VarBC Dee, 2004). For microwave observa-

tions from window channels, typically there are predictors for 10m wind speed and skin temperature that remove most of the linear component of any biases shown in the previous section. Second, the different characteristics of the background departures result in different interaction with quality control measures like the background departure check (which rejects data at a multiple of the estimated total error of the background departures) and variational quality control (VarQC; Anderson and Järvinen, 1999). This means that a different sample of observations will be assimilated depending on the chosen model. Third, when the data assimilation system is cycled, the background atmospheric state will be different in the different experiments. Fourth, there are possible side effects through the observation error model, which depends on simulated observations. To initially isolate the impact of changing bias correction, while avoiding the second, third and fourth issues, Sec. 5.1 continues to analyse the special same-background experiments as used in previous sections. Then the full impact of the change in long cycled data assimilation experiments is evaluated in Sec. 5.2.

5.1 Same-sample, same-background comparisons

Figure 10 summarises the same GMI data that was seen in Sec. 4, but now looking at the bias correction (panels a and b) and finally the bias corrected departures (c and d). In these special single-cycle experiments, the background was the same for both models, but the bias corrections were appropriate to the surface emissivity model, and have been taken from those spun up in the cycling data assimilation experiments described in the next section. Note also that the investigation here uses the screened sample (identical to the screened sample in earlier sections) representing the data that gets passed to 4D-Var, although in some cases it is only passively monitored rather than actively assimilated. Also to be noted is the change in channel notation, here using an approximate and often standardised frequency and polarisation to emphasise commonalities between different sensors. For example the 18.7 GHz V-polarised channel of GMI is noted as 19v.

Broadly, the standard deviation of the bias correction (Figure 10a) is reduced in most channels, resulting from the clear improvements in the temperature and wind speed dependence seen at these frequencies in the previous section (Figs. 6 and 8) which means the bias correction does not need to work so hard. However, the mean bias correction (Fig. 10b) is generally more positive with SURFEM-ocean, which in most cases also means larger, and this is especially clear in the mid-frequency H polarisation, i.e. channels 37h and 89h, coming from the general decrease in H-polarised emissivity in these channels when going from FASTEM-6 to SURFEM-ocean (Fig. 1).

Finally, the standard deviation of the bias corrected departure $d = y_o - b - y_b$ is also shown in Fig. 10, with b the bias correction from VarBC. The standard deviation is mostly indistinguishable between FASTEM-6 and SURFEM-ocean in terms of the absolute value (panel c) although in practice there are detectable small changes (panel d). The standard deviation of departures is around 0.01 K smaller for channels at 10 GHz and up to 0.3 K larger for 37h and 89h. The bias correction should have removed any changes that are linear functions of wind speed and temperature, or which generate an overall offset. Hence the increase in standard deviation suggests that there are biases or errors that are not linear functions of these predictor variables and which have got smaller at low frequencies and larger at high frequency H-polarisations.

To further examine the residual biases (e.g. biases after bias correction) in GMI as a function of wind speed, Fig. 11 uses the same all-sky but screened sample as Fig. 6 but now applies bias correction. Broadly, the V-polarised bias corrected departures from SURFEM-ocean have no residual (i.e. non-linear) bias as a function of wind speed. Biases in the V channels are typically well within +/- 1.0 K except at wind speeds above 15 ms^{-1}. However, the H-polarised channels retain quite large residual

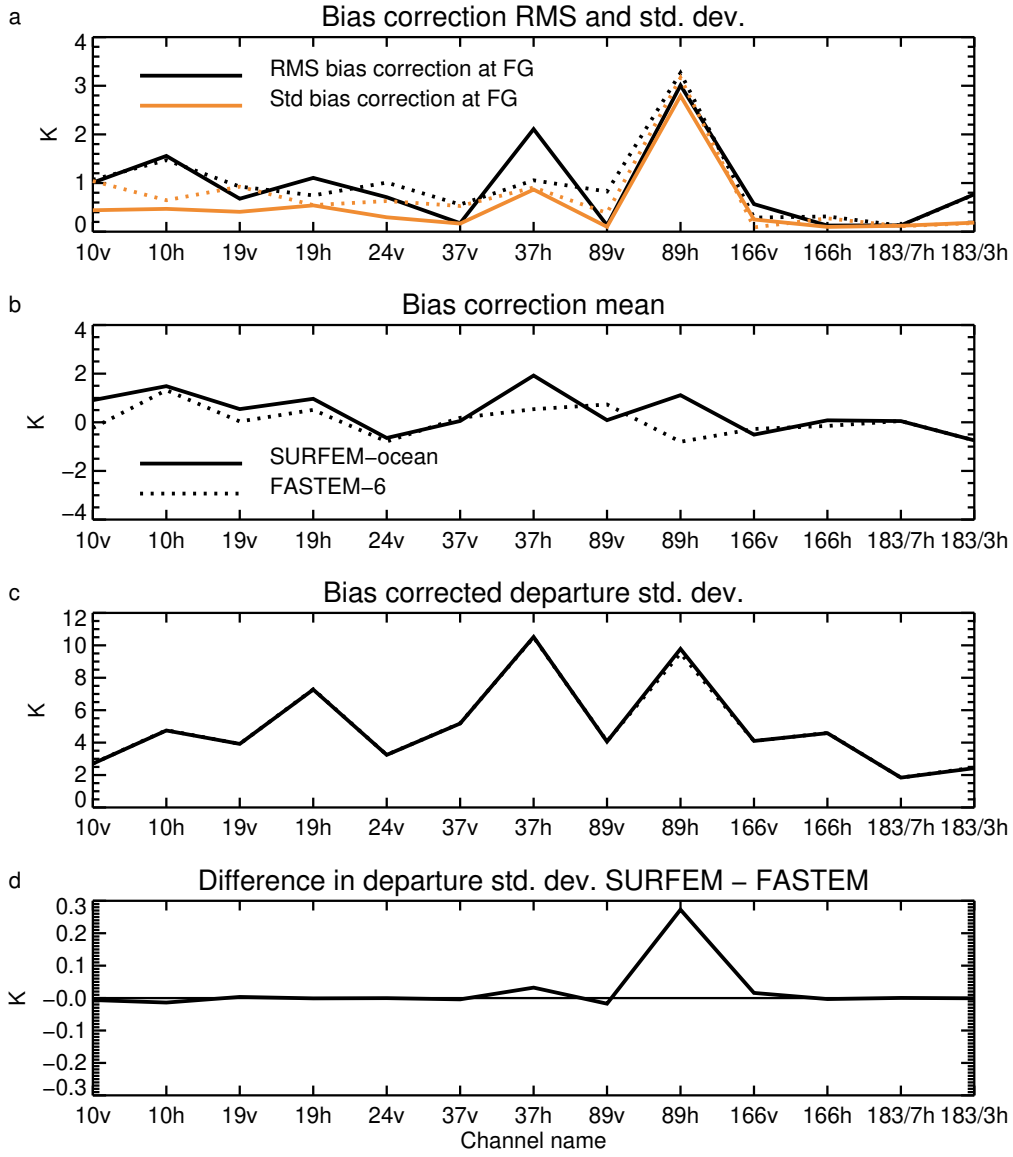

Figure 10: Summary of changes in bias correction and bias corrected departures using bias corrected and screened GMI observations in the assimilation windows on 15th June 2020, in other words showing the changes in the departures available to 4D-Var.

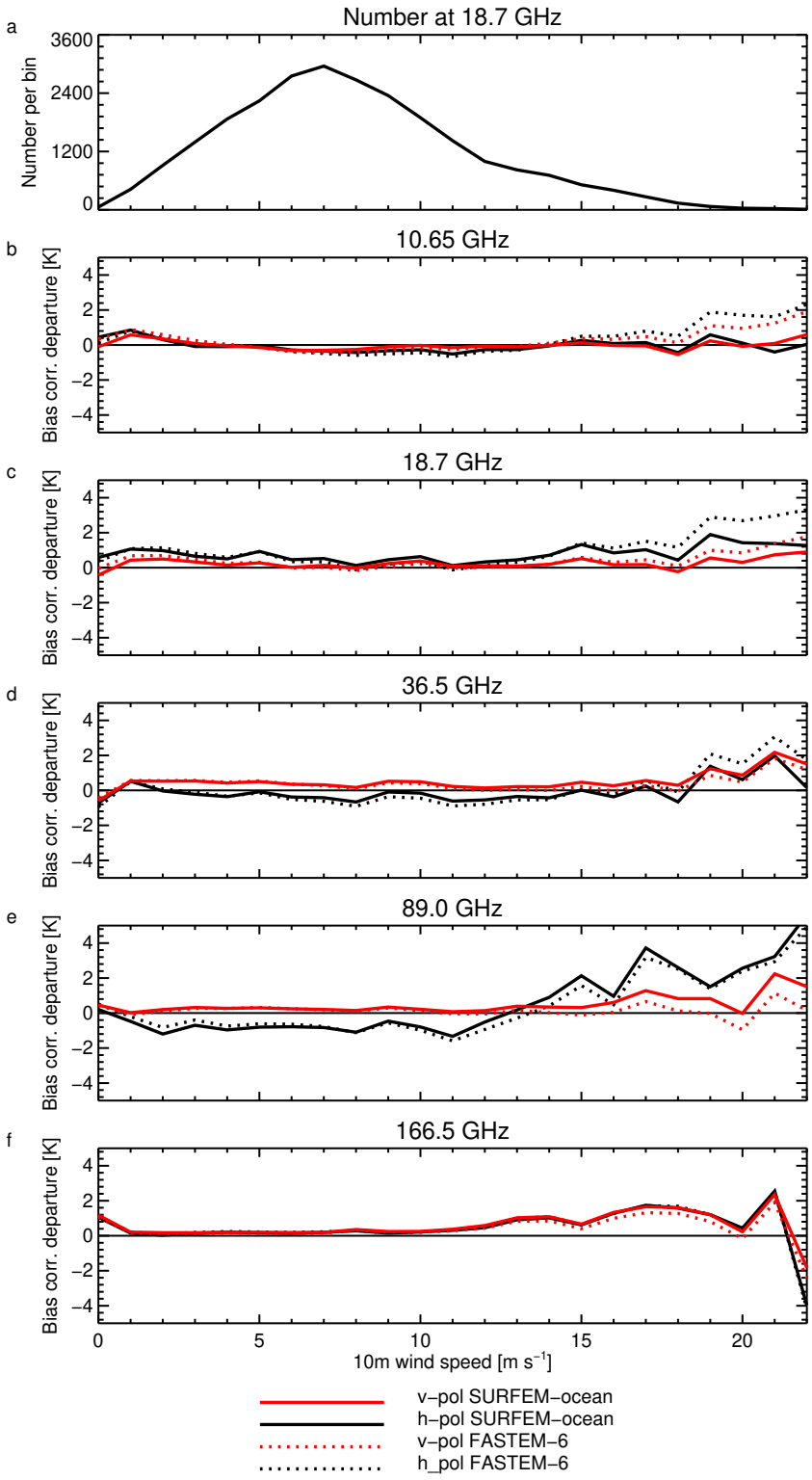

Figure 11: As Fig. 6 using a screened sample, but using bias corrected observations in the assimilation windows on 15th June 2020, in other words showing the changes in the departures used by 4D-Var.

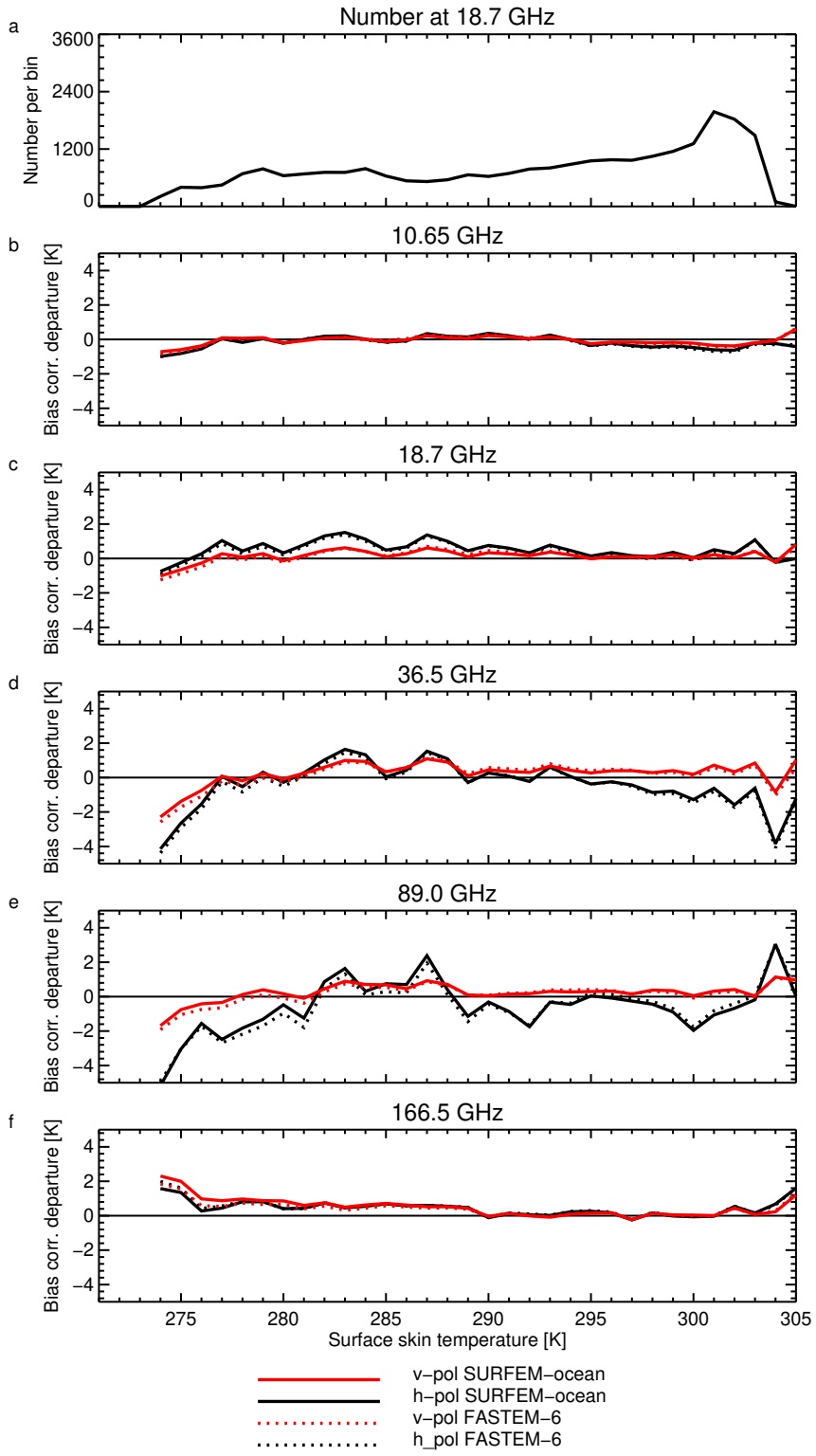

Figure 12: As Fig. 11 using a screened sample with bias corrected observations, but stratifying the bias against temperature.

biases, up to around -1 K even within the bulk of the data at 5 to 10 ms^{-1} for 89h. Broadly consistent with the change in standard deviation of bias corrected departures, the size of the residual biases is generally smaller in SURFEM-ocean at 19 GHz and below, but larger at 89.0 GHz, compared to FASTEM-6.

Figure 12 shows the bias corrected departures as a function of skin temperature. In general the changes are not large, though for some frequencies and polarisations there are small increases in bias at lower temperatures. These likely corresponding to residual effects from the clearly increased departures before bias correction at these temperatures (Fig. 8). However, the bias correction, with its skin temperature predictor, appears to have corrected most of the increased bias as a function of skin temperature.

This section now examines the effect of going to SURFEM-ocean on other microwave sensors used at ECMWF. Figure 13 shows that AMSR2 has very similar results to GMI. AMSR2 also uniquely demonstrates the impact of SURFEM-ocean around 6 - 7 GHz, where the standard deviation of departures is reduced by around 0.02 K, due to similar improvements in wind speed and temperature dependence that have been examined for GMI simulations at 10 GHz.

Figure 14 shows the results for SSMIS (Special Sensor Microwave Imager Sounder; Kunkee *et al.*, 2008) on satellite DMSP-F17. The imager channel results are similar to those for GMI and AMSR2 at mid and high frequencies, with larger standard deviation of bias correction and of corrected departures at 37h, 89h and 150h especially. The channels around 50 GHz, being H-polarised, follow this pattern too, especially 50.3h. However, there are some small improvements in the standard deviation of corrected departures at 89v, similar to what was seen with GMI. The humidity sounding channels around 183 GHz are mostly unaffected, due to the fact that only locations with limited sensitivity to the surface are allowed in the screened sample.

Figure 15 shows the summary for AMSU-A on Metop-C. As was seen in the earlier analysis on departures without bias correction, SURFEM-ocean generates more positive biases than FASTEM-6 in most scan positions. Absolute biases get larger near nadir (Fig. 9) at 31v, 50.3v and 89v especially. This leads to larger bias corrections in these channels (Fig. 15a and b) and larger residual errors, meaning larger standard deviations of bias-corrected background departures. The largest increases are 0.01 K in 50.3v and 0.06 K at 89v. The standard deviation of bias corrected departures is also fractionally larger for 52.8v and 53.6h at 0.003 K and 0.002 K respectively. The latter also shows up as a statistically significant deterioration in the fit to the 53.6h channel (channel 5) on the observation monitoring plots for AMSU-A (Sec. 5.2).

Finally, Fig. 16 shows the summary for MHS on Metop-C, with similar behaviour to AMSU-A in the 89v channel, with larger bias corrections and larger standard deviations after bias correction. The changes in the 183 GHz channels are not visible, similar to those for SSMIS.

Note that this summary has included passively monitored channels, but the impact of SURFEM-ocean changes on the data assimilation depends only on the active channels. For microwave imagers, the H-polarised 37h and 89h channels are not used (Geer *et al.*, 2022). The 89v channels of AMSU-A and MHS are also not assimilated (Duncan *et al.*, 2022a) and neither are any 50 GHz channels on SSMIS, or the 50.3v and 52.8v channels on AMSU-A. This means that the channels with the largest increases in departure standard deviation are not actually assimilated.

5.2 Full cycling results

The move from FASTEM-6 to SURFEM-ocean was tested for its forecast impact in experiments based on two periods, 2nd June 2020 to 31st August 2020 and 2nd December 2020 to 28th February 2021.

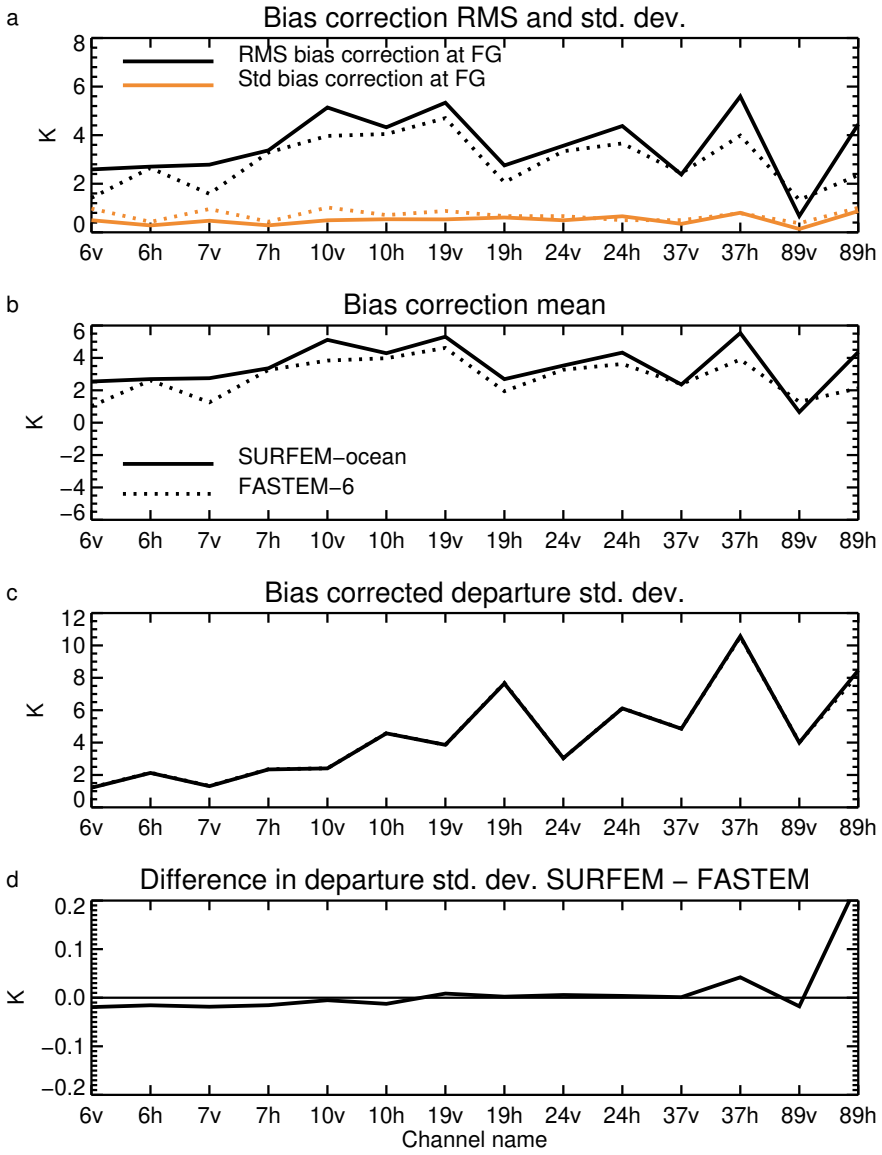

Figure 13: As Fig. 10 but for AMSR2.

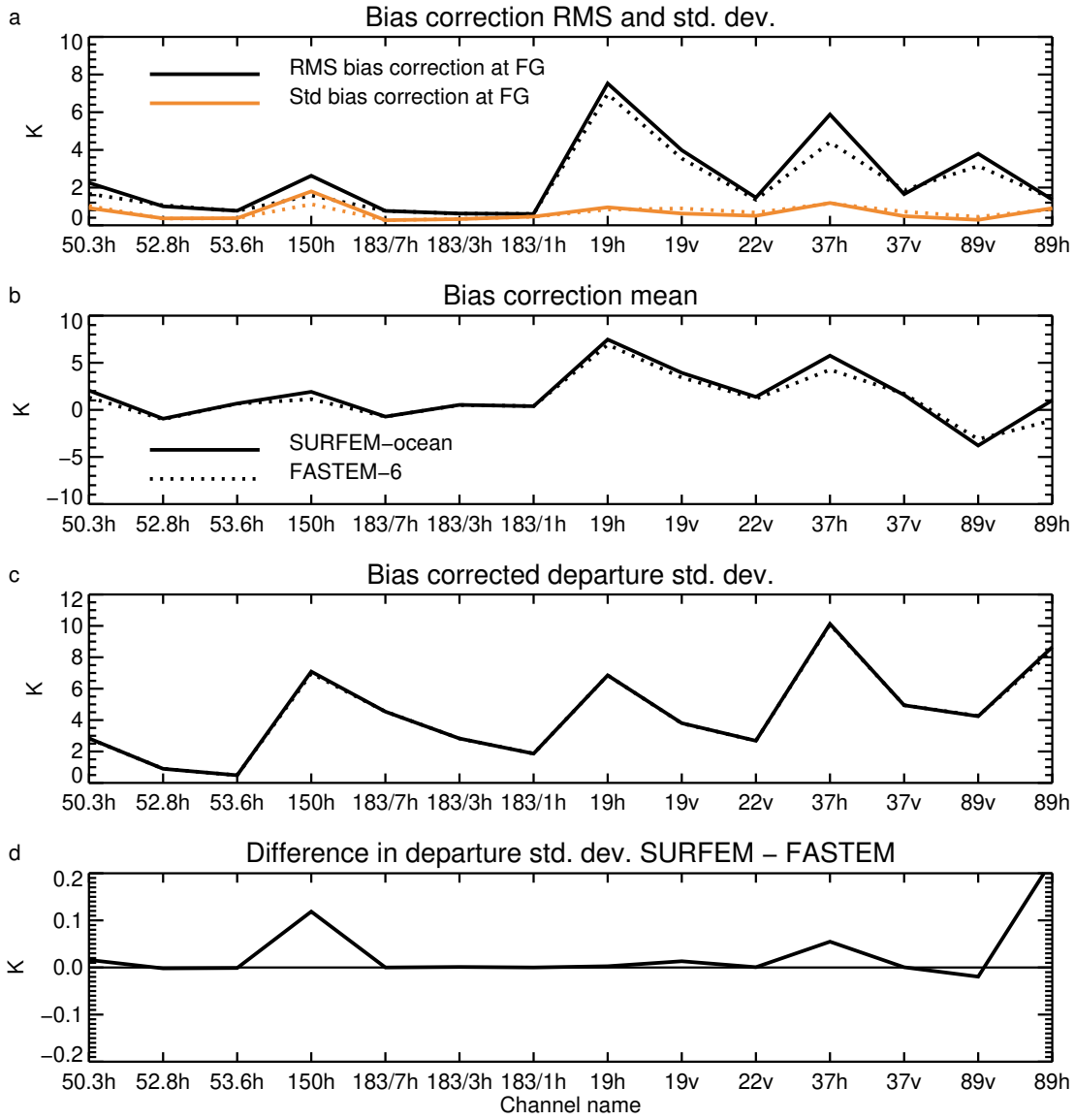

Figure 14: As Fig. 10 but for SSMIS on DMSP-F17.

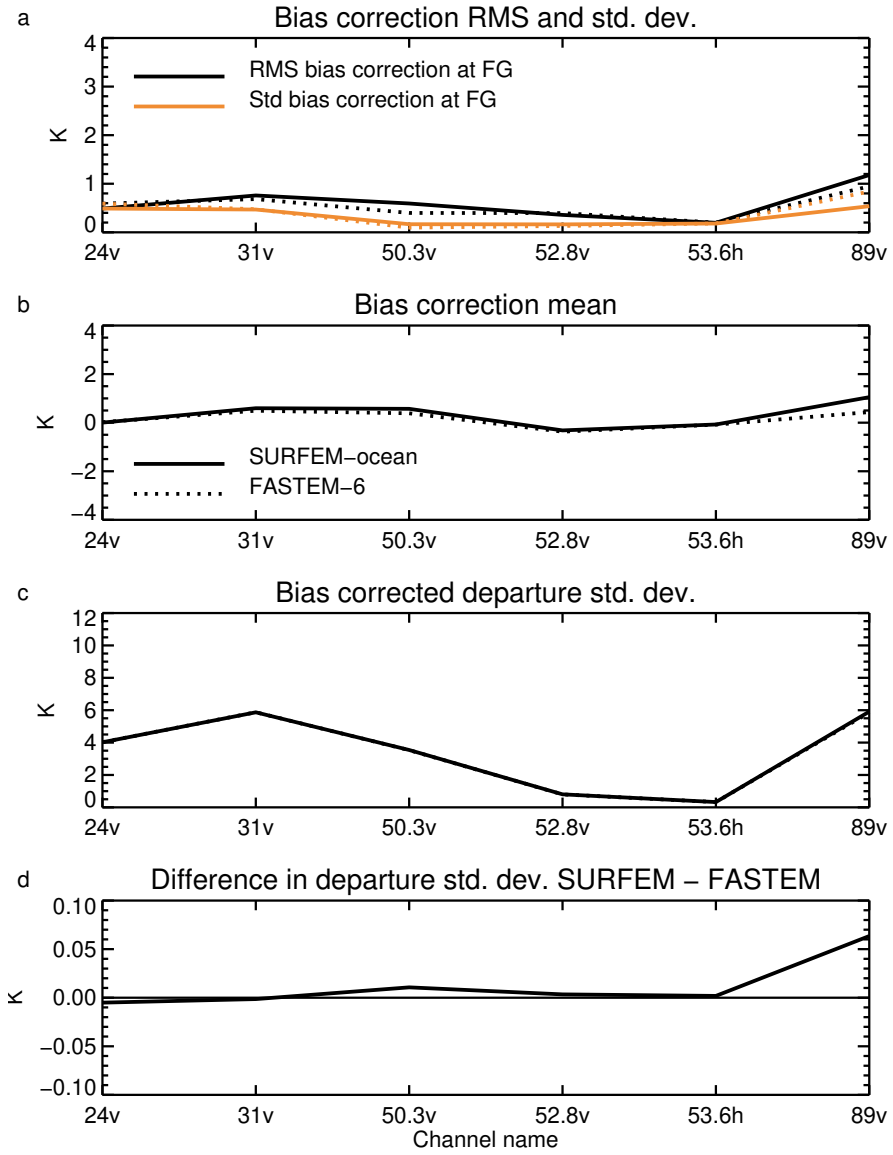

Figure 15: As Fig. 10 but for AMSU-A on Metop-C

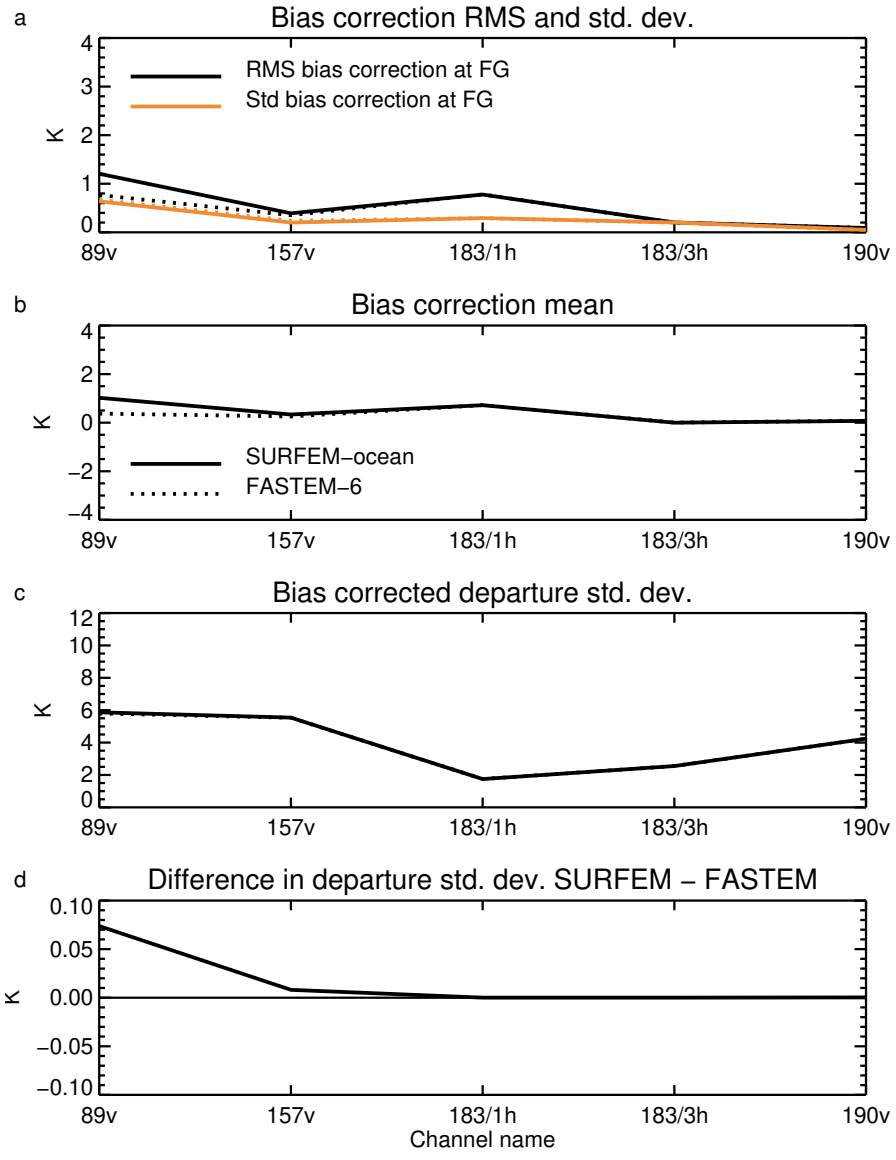

Figure 16: As Fig. 10 but for MHS on Metop-C

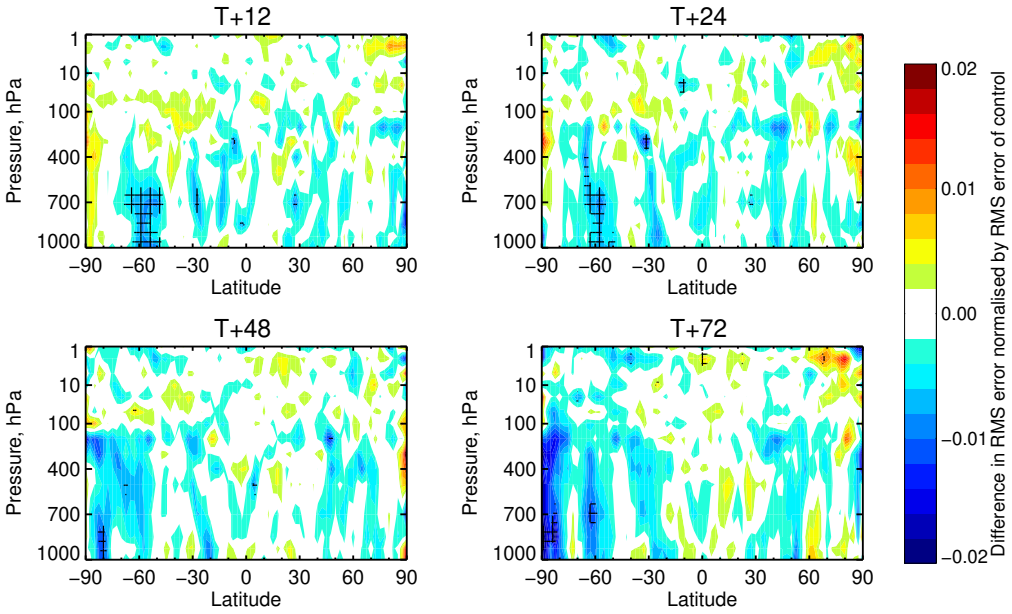

Figure 17: Difference in RMSE of vector wind (VW) error between SURFEM-ocean and FASTEM-6 experiments, normalise by the RMSE of the FASTEM-6 experiment. Verification is against own-analysis. Cross-hatching shows statistical significance at the 95% confidence level based on 20 independent tests per panel. Captions T+N describe the forecast time N in hours.

In the results presented here, these two experiments have been combined, but the first 8 days have been removed for spinup. The experiments are based on the standard testing configuration at TCo399 (about 25 km horizontal resolution) with a 12 hour assimilation window. Background errors are held fixed between the two experiments and come from a separate ensemble data assimilation experiment based on the cycle 48r1 configuration. The configuration of the FASTEM-6 (control) experiment is as cycle 48r1 but with various upgrades intended for 49r1. For the all-sky microwave observations, the cycle 48r1 configuration is detailed by Geer *et al.* (2022). The upgrades on top of this include RTTOV v13.1 (scientifically neutral), changes to SSMIS usage and assumed convection fraction in the all-sky observation operator (Scanlon *et al.*, 2023), activation of AMSU-A imager channels (Duncan *et al.*, 2022a), 50 km superobbing and reduced thinning of MHS and MWHS2 (Duncan *et al.*, 2023), and a move from 80 km to 40 km superobbing for the microwave imagers. The experiment that tests SURFEM-ocean moves to RTTOV v13.2 and activates SURFEM-ocean as the only scientific change.

The move to SURFEM-ocean from FASTEM-6 appears to reduce forecast errors. Figure 17 shows the impact on vector wind errors, but similar results are seen in geopotential height and temperature. The clearest impact at T+12 and T+24 (T+N where N is the forecast length in hours) is in the lower troposphere around 60°S. At longer forecast lead times of T+48 and T+72, the impact spreads and dissipates across the southern high and mid-latitudes. Figure 18 shows the regional impact on total column water vapour (TCWV) forecasts, which is beneficial in the first 2–3 days of the forecast with statistical significance in the southern hemisphere and tropics. This summarises improvements that are also seen in the relative humidity fields between the surface and 850 hPa. There are also regional mean changes in the forecast fields in the lower troposphere, at 1000 hPa reaching around ±0.5 % in relative humidity and ±0.05 K in temperature (not shown) which likely result from the changes in the pattern of residual biases (i.e. those that are not corrected by VarBC.)

Figure 19 shows the impact of the upgrade to SURFEM-ocean on the fit to GMI and AMSU-A obser-

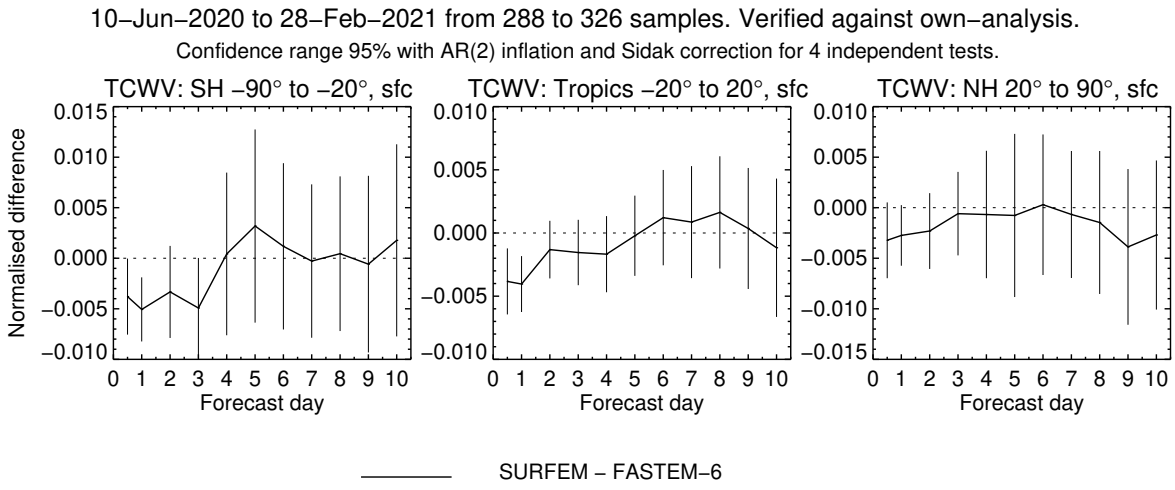

Figure 18: As Fig. 17 but showing the difference in TCWV RMSE aggregated over regions as a function of forecast range. Error bars show the statistical significance range at the 95% confidence level based on 4 independent tests in the figure, and correcting for time correlations using an autoregressive AR(2) model.

vations. This is not an independent measure of the quality of the analysis or background, but rather a diagnostic of the effect of the changes examined in previous sections. It is also affected by changes in the number of observations assimilated in the different experiments, with GMI seeing between 0.5% and 2.0% more observations being assimilated and AMSU-A usage almost unchanged (less than 0.1% different, not shown). The increase in the number of microwave imager observations appears to be at least partly due to a small increase in the average observation errors driven by the increased polarisation between 37v and 37h (Fig. 1) which affects the observation error model (Geer and Bauer, 2011) and is discussed further in Sec. 5.3. Hence, GMI shows an increased standard deviation of analysis and background departure in almost all channels, reaching nearly 2.0%, but this must come mainly from the increased data usage, since the same-sample comparison in Figure 10d shows the active GMI channels are mostly unchanged. Impact on other microwave imagers (e.g. GMI and AMSR2) is similar.

Figure 19 shows that AMSU-A fits are degraded by 0.5% in channel 5, corresponding to 53.6h, which sees small but detectable degradation in fit, likely associated with the larger near-nadir biases that are seen more clearly in other mid frequency AMSU-A channels (Fig. 9). However, there is slightly improved fit to the stratospheric AMSU-A channels (9 – 14) in the analysis. Fits to ATMS (not shown) are similar, and its humidity-sounding channels show improvements in the analysis too

Figure 20 summarises the impact on the fit to independent observations in the the analysis. For IASI, fits to channels from around 720 to 820 cm^{-1} improve by up to about 0.5% at analysis and by 0.1% at background. These channels are sensitive to the surface, lower-tropospheric temperature and moisture. Most likely this indicates that lower tropospheric moisture is in better agreement with IASI. Fits to channels from around 1400 to 1550 cm^{-1} are also improved in both analysis and forecast, indicating improved mid and upper-tropospheric humidity. Broadly similar impacts are seen for other infrared sensors in the analysis (not shown). Fits to the atmospheric motion vector winds are also improved in

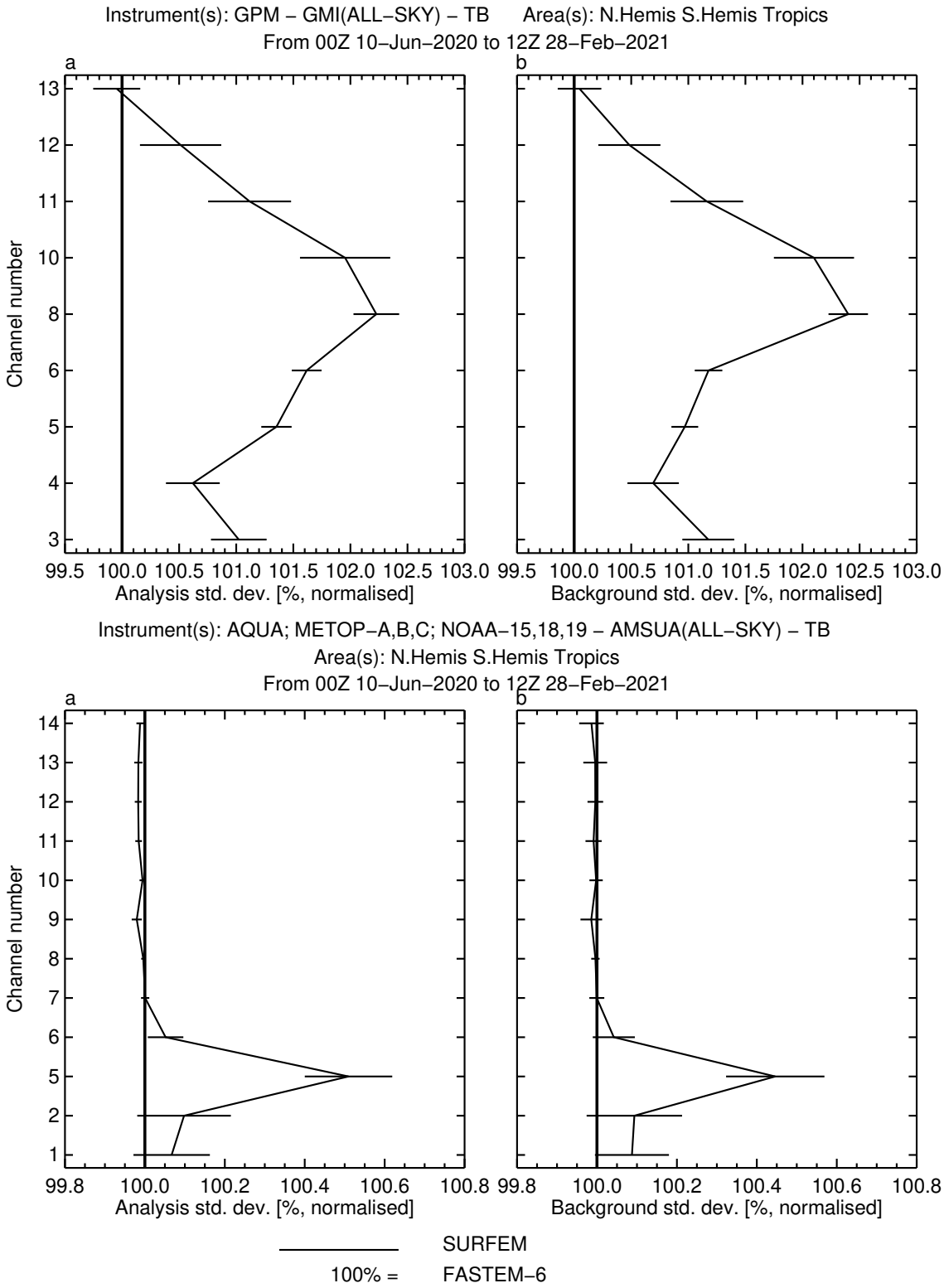

Figure 19: Normalised change in analysis (left) and background (right) bias corrected departure standard deviation for actively assimilated channels of GMI (top) and AMSU-A (bottom). Error bars show the statistical significance range at the 95% confidence level and the results are based on a global sample of observations aggregated over two experiment periods of around 3 months each.

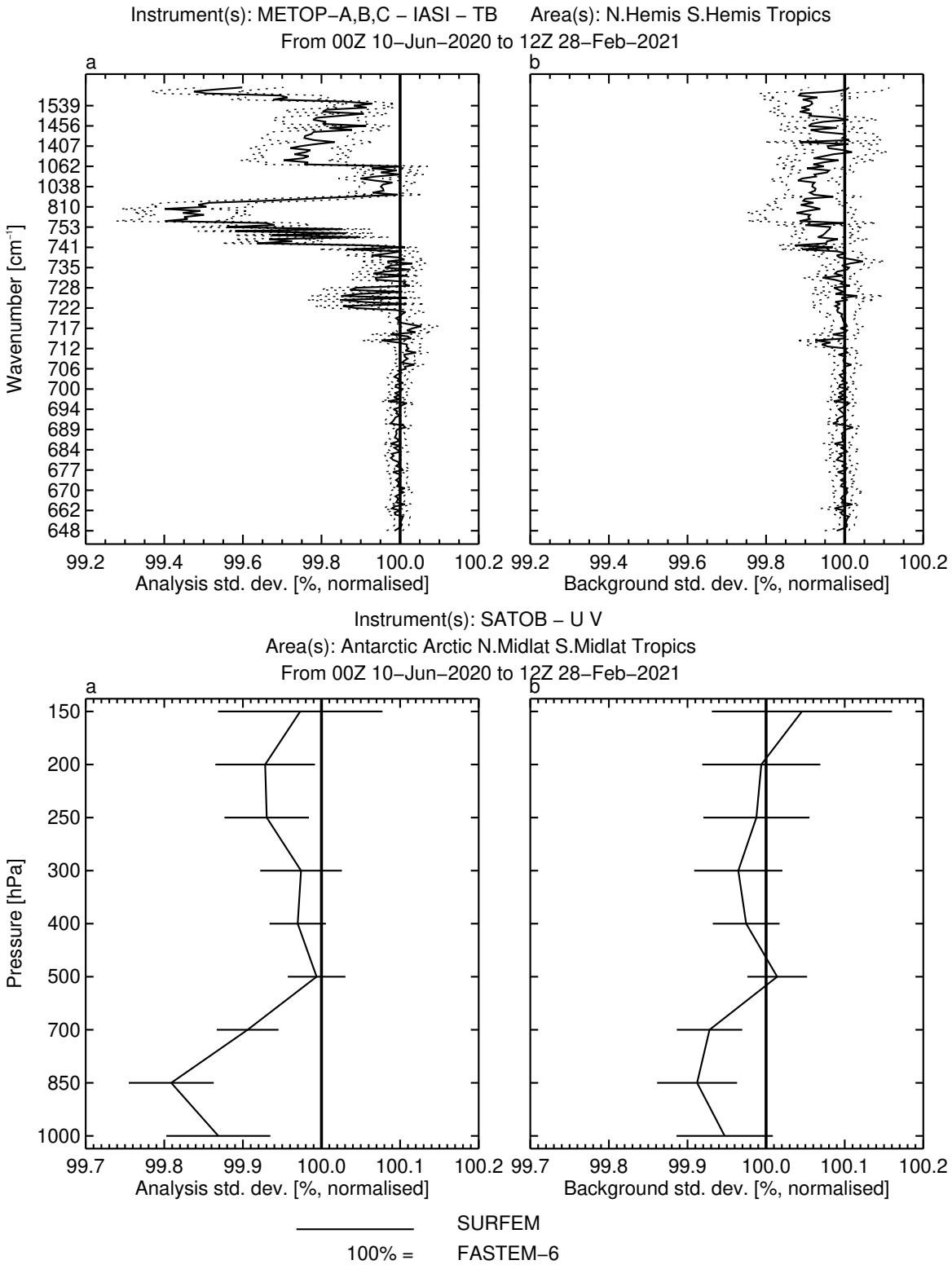

Figure 20: As Fig. 19 but for IASI (top) and atmospheric motion vectors (SATOB, bottom).

both analysis and background, with the largest impact at 700 hPa and 850 hPa. Also, and not shown, radio occultation fits also improve in the stratosphere in the analysis, which could be interpreted as fewer incorrect gravity waves being generated by the assimilation of all-sky microwave imager observations. These results confirm the picture in the analysis-based verification, showing that water vapour, wind and temperature analyses and 12 h forecasts are improved by going to SURFEM-ocean.

5.3 Mechanism for forecast improvements

In general, the standard deviation of background departures after bias correction has stayed the same or got a little worse between FASTEM-6 and SURFEM-ocean, at least in the channels at 19 GHz and above that are actually being assimilated (e.g. Fig. 10). Hence the mechanism for the forecast improvements is not immediately obvious. Figure 21 investigates. Panel a shows the surface wind speed at GMI locations and panel b the change in absolute background departure in the 19v channel, $|d_{\mathrm{exp}}| - |d_{\mathrm{control}}|$. Generally the reductions in absolute departure (blue colours) are most prevalent in the southern hemisphere in areas of wind speed above 10 m s^{-1}, where biases have clearly been reduced (Fig. 11). However, there are also many features in red where the absolute departure has got larger, likely corresponding to regions of lower wind speed where there are some increases in the bias (Fig. 11). A relatively balanced mix of improvements and degradations is consistent with the fact that the standard deviation of departures stay roughly constant at 19v (Fig. 10).

However, the impact on the analysis is controlled in part by the assigned observation error. The observation errors for microwave imagers depend on the amount of cloud, as indicated by the normalised 37 GHz polarisation difference (Geer and Bauer, 2011). Hence Fig. 21c shows the change in absolute normalised departure, but using the observation error in the control $\sigma_{\mathrm{control}}$, so that the figure shows $(|d_{\mathrm{exp}}| - |d_{\mathrm{control}}|)/\sigma_{\mathrm{control}}$. This normalisation seems to reduce the visual impact of the red areas compared to the blue, in other words the areas where the departures get larger seem to be preferentially cloudy areas, where the observation errors are larger. This also seems to be consistent with the way that biases (before bias correction) are present when the cloudy sample is included but are mostly eliminated when it is removed (contrast Figs. 6 and 7).

Figure 21d shows the change in absolute normalised departure when using the correct errors for each experiment, $|d_{\mathrm{exp}}|/\sigma_{\mathrm{exp}} - |d_{\mathrm{control}}|/\sigma_{\mathrm{control}}$. Here, the red areas almost vanish but the blue areas spread over much of the map. This indicates, as mentioned earlier, that the prescribed observation errors got slightly smaller with SURFEM-ocean. This is because the polarisation difference at 37 GHz has got a little larger (Fig. 1), which makes the cloud index apparently more cloudy and increases the observation error. This is an unintentional side effect of the upgrade to SURFEM-ocean. Observation errors can increase by up to 40% in some areas but generally the increases are limited to below 20% (not shown). In the normalised departures, the predominant reductions are found in areas with wind speed around 15 m s^{-1}, for example in the central South Pacific and South Atlantic.

The results in Fig. 21 are broadly consistent with other assimilated microwave imager channels, not shown here. In some channels, the filtering mechanism is dominant in terms of generating smaller normalised departures. In others it is mainly the unintended increase in observation errors. Without performing dedicated experiments, it is not possible to say which mechanism is dominant overall, but likely both mechanisms are important. Also, a mechanism that is harder to test is the filtering properties of the background errors or the atmospheric forecast model, either of which could possibly benefit disproportionately from the reduced normalised absolute departures in high wind speed areas. Hence the improved wind and moisture forecasts in the first few days of the forecast, particularly at high latitudes (Fig. 17) almost certainly benefit from the filtering effect of the observation errors as well as the

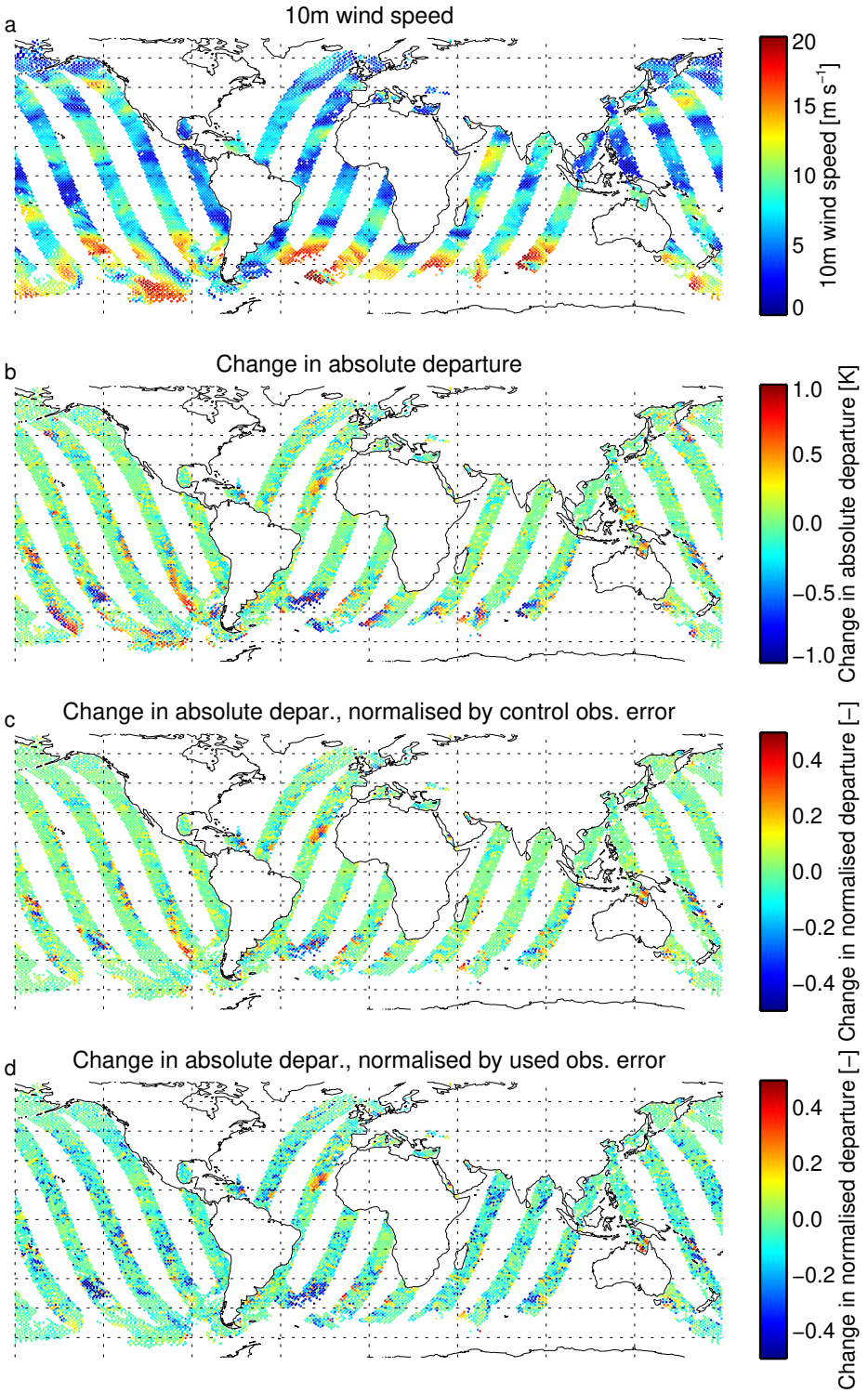

Figure 21: Illustrating the likely mechanism driving forecast improvements from the SURFEM-ocean upgrade, based on the actively assimilated sample of GMI channel 19v data in the 12 UTC window on 15th June 2022: a) 10m wind speed; b) Change in absolute background departure; c) Change in absolute background departure normalised by the control observation error; d) Change in absolute normalised background departure.

increased observation errors, and possibly benefit from other filtering effects too. Although it would have been possible to retune the observation errors, and to perform experiments in which the observation errors did not change, this would have been a large effort and was not considered worthwhile.

AMSU-A and MHS were also investigated for a change in observation errors. Figure 22 shows the effect of moving from FASTEM-6 to SURFEM-ocean on the scattering index (SI) used by MHS and the liquid water path retrieval used by AMSU-A (Geer and Baordo, 2014; Duncan *et al.*, 2022b). This change has had little effect on the LWP predictor and slightly reduced the SI.

6 Conclusion

This report has examined the activation of the SURFEM-ocean fast microwave surface emissivity model as part of the observation operator for passive microwave observations in the IFS, as a replacement for FASTEM-6. SURFEM-ocean is a new model that comes out of international activities to develop the new reference surface emissivity model PARMIO (English *et al.*, 2020; Dinnat *et al.*, 2023; Kilic *et al.*, 2023). The upgrade improves forecast scores in the lower troposphere in the southern hemisphere high latitudes out to around day 3. It also prepares the IFS for future instruments making measurements above 200 GHz, such as the ESA Arctive Weather Satellite (AWS, `https://www.esa.int/aws`) and EUMETSAT Ice Cloud Imager (Eriksson *et al.*, 2018), which are due for launch in 2024 and 2025. It also sets up the system for future instruments making full polarimetric measurements with sensitivity to wind speed and direction, such as the Weather System Follow-on – Microwave (WSF-M; Draper *et al.*, 2023) and CIMR (Copernicus Imaging Microwave Radiometer; Kilic *et al.*, 2018).

Apart from the improved polarimetric capabilities and ability to operate above 200 GHz, the main benefit of SURFEM-ocean over FASTEM-6 is the improved wind speed and temperature dependence of the surface emissivity at lower microwave frequencies (6 – 24 GHz). At 6 – 10 GHz, fits to observations are clearly improved. These channels are not yet assimilated in the IFS, but they will be used for skin temperature estimation in the near future (e.g. McNally *et al.*, 2022). The reduced errors should help provide better skin temperatures. However, for channels at 19 GHz and above that are currently assimilated, the pattern is more mixed. For example, improved fits to observations are seen in areas of high wind speed and colder surface temperatures at frequencies like 19 GHz, but fits to observations get worse at other locations at 19 GHz and more generally at higher frequencies.

For the assimilated channels, given that the global standard deviation of bias-corrected background departures is generally increased with SURFEM-ocean, the mechanism for forecast impact needs some explaining. One factor is likely a filtering effect within the data assimilation system, whereby the improved fit to observations in cold, high wind speed areas is able to contribute to improved forecasts, whereas the poorer fit in other areas has less impact. One part of this possible effect has been demonstrated, whereby observation errors are typically smaller in the areas where SURFEM improves the fit to observations, but observation errors are larger in the areas where it does not. Given that observation errors are designed to be higher in cloudy areas, this suggests that the improvements in SURFEM are found preferentially in clear-sky areas. Other filtering possibilities may come through the background errors and through the sensitivity of the forecast model to initial condition errors.

The apparent improvement in forecasts going to SURFEM-ocean also likely comes from an unintended increase in the observation errors assigned to microwave imagers, driven by the increased polarisation at 37 GHz in the SURFEM-ocean model. The increases in observation errors are generally less than 20%, but this does reduce the weight given to the observations in the data assimilation. The difficulty of interpreting apparent changes in short-range forecast errors in the context of changes in the weight

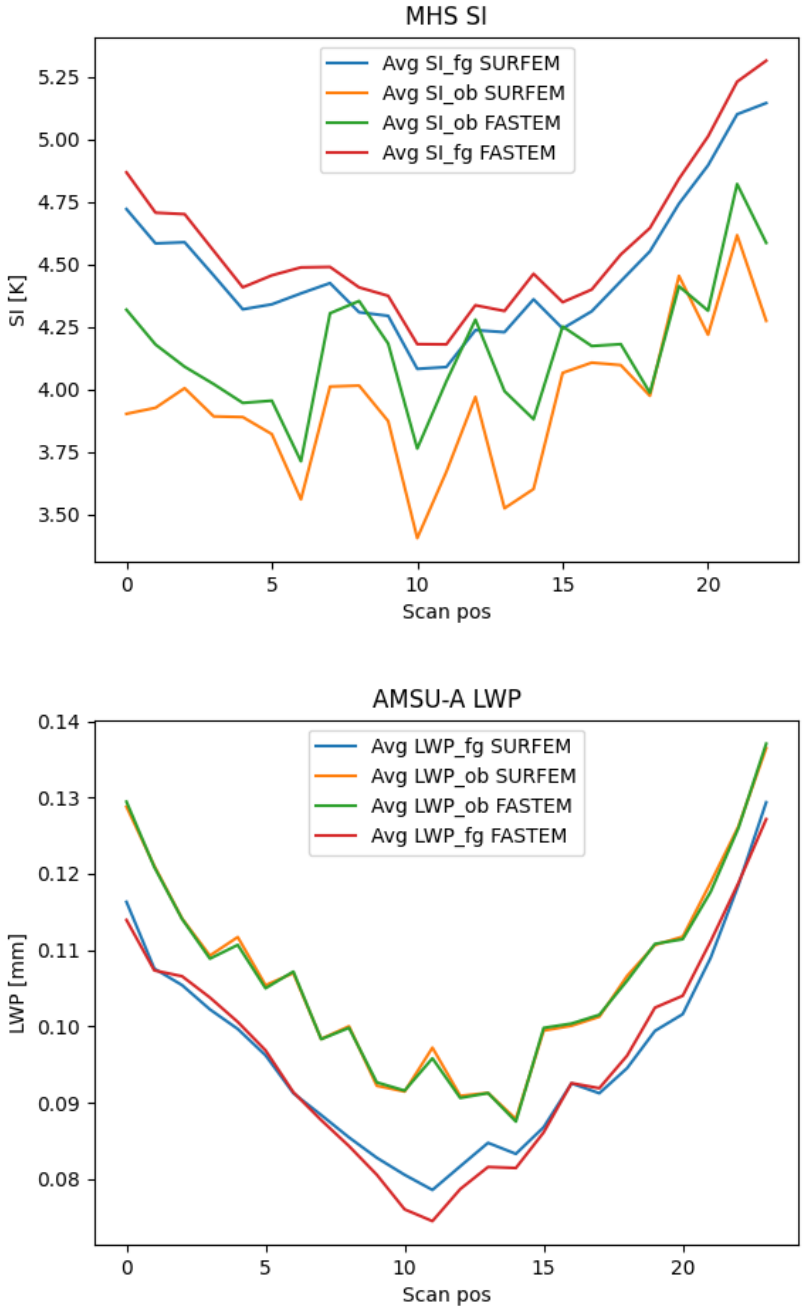

Figure 22: Mean of predictors for the observation error models of MHS (top) and AMSU-A (bottom), namely the 90-150 GHz scattering index (SI) and a liquid water path (LWP) retrieval. These are computed for both background (FG) and observation (OB).

assigned to observations is a long-running issue (e.g. Geer and Bauer, 2010). This means it is difficult to determine how much of the apparent improvements in the forecasts come simply from the reduced size of the normalised departures, rather than any true improvement in the forecast quality. Luckily, there is no similar side-effect on the observation error model for the microwave sounders, which use cloud predictors that are not affected much by the change. It was not considered worthwhile to investigate the effect further or to attempt retuning the observation errors for microwave imagers, especially given the nominally improved forecast scores.

The main degradation in the fit to observations when going from FASTEM-6 to SURFEM-ocean is associated with a general reduction in surface emissivity in mid and high frequency channels. These changes are seen in the microwave imagers (with zenith angles around 53°) particularly in the H-polarised channels at 37, 89 and 150-166 GHz. In cross-track scanning microwave sounders, similar changes are seen particularly in the 31v and 89v imaging channels and the 50.3v, 52.6v and 53.6h imaging and temperature sounding channels, with the largest changes near nadir. The reduction in surface emissivity is strongest for high wind speeds and for low temperatures. The systematic reduction in surface emissivity going from FASTEM-6 to SURFEM-ocean is also clearly seen in Kilic *et al.* (2023, their Figs. 15 and 16), as a phenomenon extending between around 20 GHz and 200 GHz. The generally increased biases against GMI and AMSR2 that result from this change in surface emissivity are also seen in that work (their Fig. 10, biases increased by up to around 2.0 K).

In the IFS, the decreased surface emissivity in mid and high-frequency microwave imager H-polarisations at 53° and at similar frequencies near nadir for microwave sounders also results in more positive and generally larger biases between observations and model simulations. These biases are not fully adjusted by the VarBC bias corrections, which only have linear models available to correct any bias as a function of skin temperature and 10m wind speed. Residual errors are increased even after bias correction and lead to a general increase in the standard deviations of bias-corrected background departures at 19 GHz and above (Fig. 10 and similar). The increases in standard deviations are largest in the microwave imager 89h channels, reaching nearly to 0.3 K. Apart from the effects already mentioned, one likely reason this does not degrade IFS forecasts is that the most strongly affected channels (such as 37h and 89h on microwave imagers, and 89v on microwave sounders) are not actively assimilated. However, the degraded performance of SURFEM-ocean in this respect does feed through to channel 5 of AMSU-A, one of the most important actively assimilated temperature sounding channels. Here, degradations of around 0.4% in analysis and background fits (Fig. 19) come directly from the upgrade to SURFEM-ocean.

To explain the changes going from FASTEM-6 to SURFEM-ocean, one aspect that can be ruled out is the change in the permittivity model for sea water from the one used in FASTEM-6 to Meissner and Wentz (2012) in SURFEM-ocean. Figure 4 shows that even had SURFEM-ocean retained the FASTEM-6 permittivity model, it would not have changed the results much. Hence the increased biases appear to largely reflect the changes in the wind speed dependence of surface emissivity.

One confounding factor for any possible increased bias in the mid and high-frequency imaging channels would be a known lack of liquid water cloud in the IFS model, particularly in cold air outbreaks (Forbes *et al.*, 2016). The mid and high frequencies are extremely sensitive to even small amounts of liquid water cloud and the biases could be explained by missing cloud liquid water at amounts often much less than 0.1 kg m^{-2}. If the generally reduced surface emissivity in SURFEM-ocean is correct, this would suggest that the missing cloud bias is even larger than previously considered. However, the strong biases in cold air outbreaks and high wind speeds (around 19 m s^{-1}) are not fully eliminated by going from FASTEM-6 to SURFEM-ocean, even at frequencies like 10 GHz where the observations are least affected by liquid cloud. Hence this might suggest that further improvements are possible in the surface

emissivity modelling at high wind speeds, though the quality of the near-surface winds in the IFS might also be worth investigating.

Despite the mixed performance, the decision to upgrade to SURFEM-ocean is easy to make, since it supports our future use of low-frequency channels (below 19 GHz), polarimetric channels, and frequencies above 200 GHz. Also, through the combination of an unintended small increase in the microwave imager observation errors and the filtering properties of the data assimilation system, the improved performance of SURFEM-ocean at high wind speeds seems to have dominated the impact on forecast quality, leading to apparently improved forecasts and improved background fits to independent observations. Hence, as a result of the benefits to current forecasts and future applications, the upgrade to RTTOV v13.2 and the activation of SURFEM-ocean have been included in the IFS cycle 49r1, which will be made operational in autumn 2024.

It is a long-held aspiration to activate the assimilation of the mid-frequency channels that are currently excluded (e.g. 37h and 89h on microwave imagers and 89v on microwave sounders) but recent testing has not shown clear positive benefits on forecasts (e.g Scanlon *et al.*, 2023; Duncan *et al.*, 2022a). These channels show particularly large departures at high latitudes, likely associated with errors in column water vapour and water cloud but also highlighting modelling errors, certainly in the lack of supercooled liquid water in the IFS in these areas, but possibly also in the surface emissivity models at high wind speeds and low sea surface temperatures. Further, it has been seen that activating microwave imager channels in cold air outbreaks as part of developments towards sea ice assimilation (Geer, 2023) has improved forecasts in the southern ocean over the first 4 days, even on top of the improvements seen going to SURFEM-ocean in the current work. Therefore, further efforts towards activating both the missing channels and the CAO regions are likely worthwhile, with a focus on possible improvements in the wind speed dependence of fast surface emissivity models, as well as efforts to address the lack of liquid water in the IFS.

Acknowledgements

Lise Kilic, Catherine Prigent, Carlos Jimenez and James Hocking are thanked for comments and discussions. Tony McNally and Andy Brown are thanked for reviewing.

References

Anderson, E. and Järvinen, H. (1999). Variational quality control. *Q.J.R. Meteorol. Soc.*, **125**(554), 697–722.

Anguelova, M. D. and Gaiser, P. W. (2013). Microwave emissivity of sea foam layers with vertically inhomogeneous dielectric properties. *Remote sensing of environment*, **139**, 81–96, URL https://doi.org/10.1016/j.rse.2013.07.017.

Bauer, P., Lopez, P., Salmond, D. and Geer, A. J. (2006). Assimilation of cloud and precipitation affected microwave radiances. *Tech. Memo. 502*, ECMWF, Reading, UK.

Berg, W., Bilanow, S., Chen, R., Datta, S., Draper, D., Ebrahimi, H., Farrar, S., Jones, W. L., Kroodsma, R., McKague, D., Payne, V., Wang, J., Wilhiet, T. and Yang, J. X. (2016). Intercalibration of the GPM microwave radiometer constellation. *Journal of Atmospheric and Oceanic Technology*, **33**(12), 2639–2654, URL https://doi.org/10.1175/JTECH-D-16-0100.1.

Bormann, N., Geer, A. and English, S. (2012). Evaluation of the microwave ocean surface emissivity model FASTEM-5 in the IFS. *ECMWF Technical Memorandum 667*.

Bormann, N., Geer, A. and Wilhelmsson, T. (2011). Operational implementation of RTTOV-10 in the IFS. *ECMWF Technical Memorandum 650*.

Cox, C. and Munk, W. (1954). Measurement of the roughness of the sea surface from photographs of the sun's glitter. *Josa*, **44**(11), 838–850, URL https://doi.org/10.1364/JOSA.44.000838.

Deblonde, G. and English, S. J. (2001). Evaluation of the FASTEM-2 fast microwave oceanic surface emissivity model. In *Tech. Proc. 11th Int. TOVS Study Conf., Budapest, 20-26 Sept 2000*, pp. 67–78, ITWG/IAMAS.

Dee, D. (2004). Variational bias correction of radiance data in the ECMWF system. In *ECMWF workshop proceedings: Assimilation of high spectral resolution sounders in NWP, 28 June – 1 July, 2004*, pp. 97–112, Eur. Cent. for Med. Range Weather Forecasts, Reading, UK, available from http://www.ecmwf.int.

Dinnat, E., English, S., Prigent, C., Kilic, L., Anguelova, M., Newman, S., Meissner, T., Boutin, J., Stoffelen, A., Yueh, S. *et al.* (2023). PARMIO: A reference quality model for ocean surface emissivity and backscatter from the microwave to the infrared. *Bull. Am. Meteorol. Soc.*, **104**(4), E742–E748, URL https://doi.org/10.1175/BAMS-D-23-0023.1.

Draper, D., Ellis, B., Carmack, C., Galantowicz, J., Lindsley, R., Mears, C., Wentz, K. and Wentz, F. (2023). Overview of the weather system follow-on – microwave (WSF-M) microwave sensor data processing software (MWSDPS). In *IGARSS 2023 - 2023 IEEE International Geoscience and Remote Sensing Symposium*, pp. 586–588, URL https://doi.org/10.1109/IGARSS52108.2023.10283384.

Draper, D. W., Newell, D. A., Wentz, F. J., Krimchansky, S. and Skofronick-Jackson, G. M. (2015). The global precipitation measurement (GPM) microwave imager (GMI): Instrument overview and early on-orbit performance. *IEEE J. Sel. Top. App. Earth Obs. Rem. Sens.*, **8**(7), 3452–3462, URL https://doi.org/10.1109/JSTARS.2015.2403303.

Duncan, D., Bormann, N. and Geer, A. (2022a). All-sky assimilation of AMSU-A window channels. *EUMETSAT/ECMWF Fellowship Programme Research Report 59*, ECMWF, Reading, UK, URL https://doi.org/10.21957/daefm16p8.

Duncan, D., Bormann, N., Geer, A. and Weston, P. (2023). Superobbing and finer thinning for all-sky humidity sounder assimilation. *Tech. Memo. 905*, ECMWF, Reading, UK, URL https://doi.org/10.21957/5c3b9c8d9f.

Duncan, D. I., Bormann, N., Geer, A. J. and Weston, P. (2022b). Assimilation of AMSU-A in all-sky conditions. *Mon. Weath. Rev.*, pp. 1023–1041, URL https://doi.org/10.1175/MWR-D-21-0273.1.

Durden, S. and Vesecky, J. (1985). A physical radar cross-section model for a wind-driven sea with swell. *IEEE Journal of Oceanic Engineering*, **10**(4), 445–451, URL https://doi.org/10.1109/JOE.1985.1145133.

English, S., Prigent, C., Johnson, B., Yueh, S., Dinnat, E., Boutin, J., Newman, S., Anguelova, M., Meissner, T., Kazumori, M. *et al.* (2020). Reference-quality emission and backscatter modeling for

the ocean. *Bulletin of the American Meteorological Society*, **101**(10), E1593–E1601, URL https://doi.org/10.1175/BAMS-D-20-0085.1.

English, S. J. and Hewison, T. J. (1998). A fast generic microwave emissivity model. In T. Hayasaka, D. L. Wu, Y. Jin and J. Jiang (Eds), *Proceedings of SPIE, 3503: Microwave remote sensing of the environment*, pp. 288–300.

Eriksson, P., Ekelund, R., Mendrok, J., Brath, M., Lemke, O. and Buehler, S. A. (2018). A general database of hydrometeor single scattering properties at microwave and sub-millimetre wavelengths. *Earth Sys. Sci.Data*, **10**(3), 1301–1326, URL https://doi.org/10.5194/essd-10-1301-2018.

Eriksson, P., Rydberg, B., Mattioli, V., Thoss, A., Accadia, C., Klein, U. and Buehler, S. A. (2020). Towards an operational Ice Cloud Imager (ICI) retrieval product. *Atmos. Meas. Tech.*, **13**(1), 53–71, URL https://doi.org/10.5194/amt-13-53-2020.

Forbes, R., Geer, A., Lonitz, K. and Ahlgrimm, M. (2016). Reducing systematic errors in cold-air outbreaks. *ECMWF newsletter*, (146), 17–22.

Geer, A. J. (2023). Joint estimation of sea ice and atmospheric state from microwave imagers in operational weather forecasting. *submitted to Quarterly Journal of the Royal Meteorological Society*.

Geer, A. J. and Baordo, F. (2014). Improved scattering radiative transfer for frozen hydrometeors at microwave frequencies. *Atmos. Meas. Tech.*, **7**, 1839–1860, URL https:/doi.org/10.5194/amt-7-1839-2014.

Geer, A. J. and Bauer, P. (2010). Enhanced use of all-sky microwave observations sensitive to water vapour, cloud and precipitation. *Tech. Memo. 620*, ECMWF, Reading, UK, URL https:/doi.org/10.21957/mi79jebka.

Geer, A. J. and Bauer, P. (2011). Observation errors in all-sky data assimilation. *Quart. J. Roy. Meteorol. Soc.*, **137**, 2024–2037, URL https://doi.org/10.1002/qj.830.

Geer, A. J., Lonitz, K., Duncan, D. and Bormann, N. (2022). Improved surface treatment for all-sky microwave observations. *Tech. Memo. 894*, ECMWF, Reading, UK, URL https:/doi.org/10.21957/zi7q6hau.

Good, S., Fiedler, E., Mao, C., Martin, M. J., Maycock, A., Reid, R., Roberts-Jones, J., Searle, T., Waters, J., While, J. *et al.* (2020). The current configuration of the OSTIA system for operational production of foundation sea surface temperature and ice concentration analyses. *Remote Sensing*, **12**(4), 720, URL https://doi.org/10.3390/rs12040720.

Johnson, B. T., Dang, C., Stegmann, P., Liu, Q., Moradi, I. and Auligne, T. (2023). The community radiative transfer model (crtm): Community-focused collaborative model development accelerating research to operations. *Bulletin of the American Meteorological Society*, **104**(10), E1817–E1830, URL https://doi.org/10.1175/BAMS-D-22-0015.1.

Kazumori, M. and English, S. J. (2015). Use of the ocean surface wind direction signal in microwave radiance assimilation. *Quarterly Journal of the Royal Meteorological Society*, **141**(689), 1354–1375, URL https://doi.org/10.1002/qj.2445.

Kilic, L., Prigent, C., Aires, F., Boutin, J., Heygster, G., Tonboe, R. T., Roquet, H., Jimenez, C. and Donlon, C. (2018). Expected performances of the Copernicus Imaging Microwave Radiometer (CIMR) for an all-weather and high spatial resolution estimation of ocean and sea ice parameters. *Journal of Geophysical Research: Oceans*, **123**(10), 7564–7580, URL https://doi.org/10.1029/2018JC014408.

Kilic, L., Prigent, C., Boutin, J., Meissner, T., English, S. and Yueh, S. (2019). Comparisons of ocean radiative transfer models with SMAP and AMSR2 observations. *Journal of Geophysical Research: Oceans*, **124**(11), 7683–7699, URL https://doi.org/10.1029/2019JC015493.

Kilic, L., Prigent, C., Jimenez, C., Turner, E., Hocking, J., English, S., Meissner, T. and Dinnat, E. (2023). Development of the SURface Fast Emissivity Model for Ocean (SURFEM-Ocean) based on the PARMIO radiative transfer model. *Earth and Space Science*, **10**, e2022EA002785, URL https://doi.org/10.1029/2022EA002785.

Kunkee, D., Poe, G., Boucher, D., Swadley, S., Hong, Y., Wessel, J. and Uliana, E. (2008). Design and evaluation of the first Special Sensor Microwave Imager/Sounder. *IEEE Trans. Geosci. Remote Sensing*, **46**, 863–883, URL https://doi.org/10.1109/TGRS.2008.917980.

Lawrence, H., Bormann, N. and English, S. J. (2020). Uncertainties in the permittivity model for seawater in FASTEM and implications for the calibration/validation of microwave imagers. *Journal of Quantitative Spectroscopy and Radiative Transfer*, **243**, 106813, URL https://doi.org/10.1016/j.jqsrt.2019.106813.

Lean, P., Geer, A. and Lonitz, K. (2017). Assimilation of Global Precipitation Mission (GPM) Microwave Imager (GMI) in all-sky conditions. *Tech. Memo. 799*, ECMWF, Reading, UK, URL https://doi.org/10.21957/8orc7sn33.

Liu, Q., Weng, F. and English, S. (2011). An improved fast microwave water emissivity model. *IEEE Trans. Geosci. Remote Sens.*, **49**, 1238–1250, doi:10.1109/TGRS.2010.2064779.

Lonitz, K. and Geer, A. (2015). New screening of cold-air outbreak regions used in 4D-Var all-sky assimilation. *EUMETSAT/ECMWF Fellowship Programme Research Report 35*, ECMWF, Reading, UK.

McNally, T., Browne, P., Chrust, M., Fairbairn, D., Massart, S., Mogensen, K. and Zuo, H. (2022). Progress on developing a new coupled sea-surface temperature analysis. *ECMWF Newsletter*, (172), 17–22, URL https://doi.org/10.21957/tm4913hs8d.

Meissner, T. and Wentz, F. J. (2012). The emissivity of the ocean surface between 6 and 90 GHz over a large range of wind speeds and earth incidence angles. *IEEE Trans. Geosci. Rem. Sens.*, **50**(8), 3004–3026, URL https://doi.org/10.1109/TGRS.2011.2179662.

Meunier, L.-F., English, S. and Janssen, P. (2014). Improved ocean emissivity modelling for assimilation of microwave imagers using foam coverage derived from a wave model. *NWP-SAF visiting scientist report, NWPSAF-EC-VS-024, available from https://nwpsaf.eu/*.

Monahan, E. C. and Muircheartaigh, I. (1980). Optimal power-law description of oceanic whitecap coverage dependence on wind speed. *Journal of Physical Oceanography*, **10**(12), 2094–2099, URL https://doi.org/10.1175/1520-0485(1980)010<2094:OPLDOO>2.0.CO;2.

Prigent, C., Aires, F., Wang, D., Fox, S. and Harlow, C. (2017). Sea-surface emissivity parametrization from microwaves to millimetre waves. *Quart. J. Roy. Meteorol. Soc.*, **143**, 596–605, URL https://doi.org/10.1002/qj.2953.

Robel, J. (2009). NOAA KLM user's guide (February 2009 revision). *Available from http://www.ncdc.noaa.gov/oa/pod-guide/ncdc/docs/intro.htm*.

Saunders, R., Hocking, J., Turner, E., Havemann, S., Geer, A., Lupu, C., Vidot, J., Chambon, P., Köpken-Watts, C., Scheck, L., Stiller, O., Stumpf, C., Borbas, E. and Brunel, P. (2020). RTTOV-13 science and validation report. *NWP-SAF report NWPSAF-MO-TV-046*, EUMETSAT NWP-SAF, Met Office, UK, URL https://nwp-saf.eumetsat.int/site/download/documentation/rtm/docs_rttov13/rttov13_svr.pdf.

Scanlon, T., Geer, A. and Bormann, N. (2023). Microwave imagers in the ECMWF-IFS: Adding further observations and improving convective anvils in the observation operator. *EUMETSAT/ECMWF Fellowship Programme Research Report 61*, ECMWF, Reading, UK, URL https://doi.org/10.21957/8542a37c46.